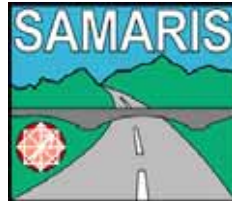


**Competitive and Sustainable Growth (GROWTH) Programme**




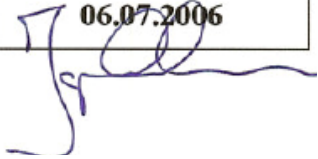
**SAMARIS**

**Sustainable and Advanced MAterials for Road InfraStructure**

**WP 14: HPRCC (High Performance Fibre Reinforced Cementitious Composites) for  
rehabilitation**

**Deliverable D26**

**Modelling of UHPFRC in composite structures**

	Name and signature	Date
Drafted:	 H. Sadouki, E. Denarié	19.12.2005 04.07.2006
Reviewed:	A. Znidaric	
Verified:	n.a.	
Validated:	n.a.	
Approved by SAMARIS Management Group:		 06.07.2006

## ABSTRACT

The extremely low permeability of Ultra-High Performance Fibre Reinforced Concretes (UHPFRC) associated with their outstanding mechanical properties make them especially suitable to locally "harden" reinforced concrete structures in critical zones subjected to an aggressive environment and to significant mechanical stresses. UHPFRC materials can be applied on new structures, or on existing ones for rehabilitation, as thin watertight overlays in replacement of waterproofing membranes, as reinforcement layers combined with reinforcement bars, or as prefabricated elements such as kerbs.

The successful rehabilitation of existing structures is a **major challenge** for civil engineers. When existing concrete needs to be replaced, *a new composite structure* formed of the new material cast on the existing substrate will result from the intervention. Both the protective function and the mechanical performance of the composite system have to be guaranteed over the planned service life. These requirements can be fulfilled by a sound understanding of the origin of deteriorations, and by proper design and application. Further, to take the full benefit of the potential of UHPFRC to rehabilitate or reinforce structures, it is often needed to get better insights of the performance of composite UHPFRC-Concrete members by means of numerical models such as finite element simulations.

The numerical modelling of multiple layer systems involves comprehensive models of the time dependent behaviour of the materials at early-age and long term. UHPFRC require special consideration of their tensile hardening behaviour.

This document gives the theoretical background, and provides validations of a constitutive model for UHPFRC under tensile loading. This model is then applied to the inverse analysis of test results in bending, and to the simulation of various configurations of application of UHPFRC in composite structural members.



## TABLE OF CONTENTS

<b>ABSTRACT .....</b>	<b>I</b>
<b>FOREWORD AND ACKNOWLEDGEMENTS.....</b>	<b>5</b>
<b>EXECUTIVE SUMMARY .....</b>	<b>7</b>
<b>1. INTRODUCTION.....</b>	<b>11</b>
<b>2. MECHANICAL BEHAVIOR OF UHPFRC UNDER QUASI-STATIC UNIAXIAL TENSILE LOADING .....</b>	<b>13</b>
<b>2.1 Introduction .....</b>	<b>13</b>
<b>2.2 Theoretical background .....</b>	<b>15</b>
2.2.1 Materials with negligible volumetric energy dissipation .....	15
2.2.2 Materials with volumetric and surfacic energy dissipation.....	16
<b>2.3 Modelling of the tensile behaviour of UHPFRC with MLS-software .....</b>	<b>18</b>
2.3.1 Scopes.....	18
2.3.2 Influence of the FE-size.....	18
2.3.3 Influence of a statistical variation of the strength .....	23
2.3.4 Combined influences of statistical distribution of tensile strength and extend of the hardening domain .....	27
2.3.5 Influence of the length of the tensile specimen on the mechanical response (size effect).....	28
2.3.6 Influence of combined statistically distributed strengths and length of the specimen .....	32
<b>3. FLEXURAL BEHAVIOUR OF UHPFRC MONOLITHIC BEAMS .....</b>	<b>37</b>
<b>3.1 Introduction .....</b>	<b>37</b>
<b>3.2 Inverse analysis with MLS.....</b>	<b>37</b>
3.2.1 Procedure.....	37
3.2.2 Four point bending plates with UHPFRC CEMTEC <sup>multiscale</sup> ® .....	38
3.2.3 Three point bending beams with UHPFRC DUCTAL® .....	41
<b>4. TIME-DEPENDENT BEHAVIOUR OF COMPOSITE UHPFRC-CONCRETE BEAMS.....</b>	<b>45</b>
<b>4.1 General .....</b>	<b>45</b>
<b>4.2 Overview of existing works .....</b>	<b>45</b>
<b>4.3 Modelling of time dependent behaviour with software MLS .....</b>	<b>46</b>
<b>4.4 Analysis of composite beams.....</b>	<b>48</b>
4.4.1 Beam geometry.....	48
4.4.2 Initial and boundary conditions .....	49
4.4.3 Material parameters .....	50
4.4.4 Finite element mesh.....	52
4.4.5 Effect of the structural boundary conditions and reinforcement bars .....	52
4.4.6 Effect of the thickness of the UHPFRCC- overlay: 30 mm.....	58
4.4.7 Composite beams with an over-depth of the overlay.....	60

**5. CONCLUSIONS.....63**

**6. REFERENCES .....65**

## FOREWORD AND ACKNOWLEDGEMENTS

This report is the fifth of a series covering all aspects necessary to the implementation of UHPFRC (Ultra High Performance Fibre Reinforced Concretes) for the rehabilitation of reinforced concrete structures, within the framework of work package (WP) 14 "HPFRCC for rehabilitation" of project SAMARIS. The other reports are:

- D13 - Report on preliminary studies for the use of HPFRCC for the rehabilitation of road infrastructure components
- D18a and D18b - Report on tests of UHPFRC in the laboratory, parts a. and b.
- D22 – Full scale application of UHPFRC for the rehabilitation of bridges – from the lab to the field.
- D25b - Guidance for the use of UHPFRC for rehabilitation of concrete highway structures
- D31 - Guidelines on selection of innovative techniques for the rehabilitation of concrete highway structures.

Contributors to WP 14 are: MCS-EPFL (contractor and WP leader), LCPC – Dr. P. Rossi (contractor), and TRL – Dr. R. Woodward (contractor).

*The original concept of application of UHPFRC for the rehabilitation of reinforced concrete structures was proposed at MCS, by Prof. Dr. E. Brühwiler, in 1999.*

The researchers who contributed to these works at MCS-EPFL under the lead of Dr. E. Denarié (WP 14 leader) and Prof. Dr. E. Brühwiler (director of MCS-EPFL) are:

- Dr. Hamid Sadouki, Senior scientist (CONCRETUM AG).
- Dr. Katrin Habel (formerly doctoral student at MCS-EPFL).
- Dr. Jean-Philippe Charron (formerly postdoctoral student at MCS-EPFL).
- Aicha Kamen (civil engineer, doctoral student at MCS-EPFL).
- John Wuest (civil engineer EPFL, doctoral student at MCS-EPFL).

*All numerical simulations presented in this report have been performed by Dr. Sadouki (CONCRETUM A.G.) who also drafted the major part of the report.*

*The finite element program used is MLS from FEMMASSE b.v, Roelfstra et al. (1997).*

*Their support of Dr. Roelfstra and Dr. Schlangen from FEMMASSE b.v. for the development and implementation of the finite element models is gratefully acknowledged.*

Finally, Dr. Pierre Rossi of LCPC-France, inventor of CEMTEC<sup>®</sup><sub>multiscale</sub> and worldwide known expert of Fibre Reinforced Concretes, proposed the original UHPFRC recipes used in this study and the concepts for their tailoring to the specific applications of rehabilitation.

Lausanne, July 5, 2006

Dr. Emmanuel Denarié





## EXECUTIVE SUMMARY

The successful rehabilitation of existing structures is a **major challenge** for civil engineers. Indeed, design of reliable and durable concrete rehabilitations is often more complex than the design of a new structure. When existing concrete needs to be replaced, *a new composite structure* formed of the new material cast on the existing substrate will result from the intervention. Both the protective function and the mechanical performance of the composite system have to be guaranteed over the planned service life.

The numerical modelling of composite systems formed of cementitious materials of different ages has three main goals:

- determination of parameters and their evolution with time that are not accessible through experimentation (eigenstresses for instance),
- inverse analysis of experimental test results to determine fundamental properties (constitutive law in uniaxial tension, heat of hydration, diffusion coefficient, etc.),
- prediction of the response for different geometries and boundary conditions, parametric studies and design.

The numerical modelling of systems with multiple layers of cementitious materials with different ages requires comprehensive models of the time dependent behaviour at early-age and long term. UHPFRC require special consideration of their tensile hardening behaviour with significant bulk energy dissipation. Further, recent works, Habel (2004), have shown the significant influence of the softening part of the tensile behaviour of UHPFRC on the structural response of UHPFRC-concrete structural members. It is thus necessary for the application of these materials in composite construction to consider a global hardening-softening model for the UHPFRC.

Inverse analyses of fracture tests on composite UHPFRC-concrete members, performed with an analytical cross sectional model, with empirical characteristic length, Habel (2004), delivered uniaxial tensile laws completely different from the response measured in uniaxial tensile tests on notched specimens. This difference can be explained qualitatively by the use of notched specimens and effect of eigenstresses among others. It also reveals the need for in depth modelling of the tensile behaviour of UHPFRC by means of finite element simulations.

*The present report is devoted to the numerical modelling of (1) the mechanical response under quasi static tensile or flexural loading of UHPFRC and (2) the thermo-mechanical behaviour of a concrete member rehabilitated by means of an UHPFRC overlay.*

More specifically, the emphasis is put on the tensile behaviour of UHPFRC and the adequate modelling of their hardening-softening response by means of Finite Element codes (Smearred Crack Model).

First, a smeared crack model of the tensile behaviour of UHPFRC is validated and applied to the modelling of the fracture of UHPFRC under tensile loading, with different configurations (statistical variation of parameters and effect of the length of the specimen). Secondly, this model is applied to the inverse analysis of various bending tests with different types of UHPFRC. Finally, the time-dependent structural response of composite UHPFRC-concrete

members (bi-material) with different geometries and degrees of restraint is determined in two different cases: UHPFRC overlay of uniform thickness and with an over depth.

Following conclusions can be drawn from the studies:

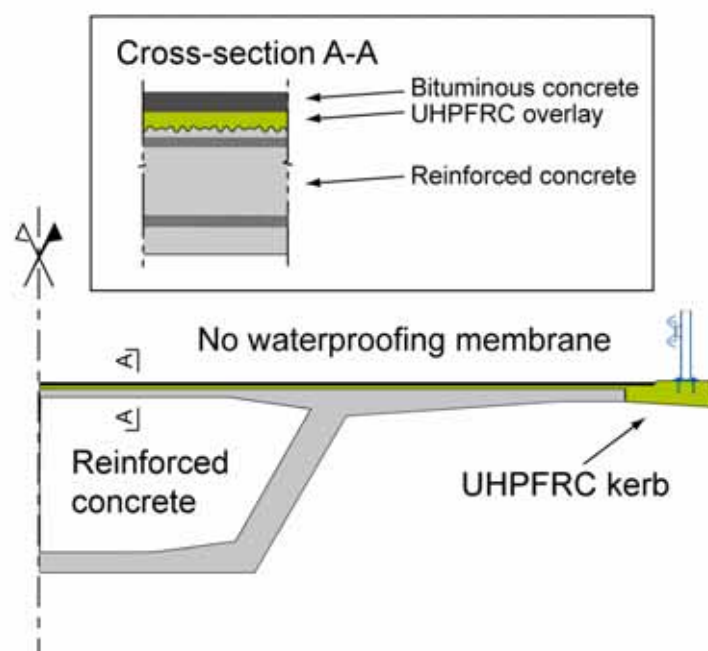
- The tensile behaviour of UHPFRC with volumetric and surfacic energy dissipation can be represented in finite element codes by a smeared crack model with adapted characteristic lengths. One length, representative of the volumetric dissipation is constant. The length related to the surfacic energy dissipation is a function of the mesh size such as to conserve the surfacic energy dissipated during the fracture of the material, according to the generalized crack band model of Bazant et Oh (1983).
- The tensile response of UHPFRC in structural members under pure tensile loading is a function of the geometry of the element (length) and the apparent specific fracture energy decreases when the specimen's length increases.
- The introduction of a statistical scatter of the parameters of the tensile model of UHPFRC has a significant impact on the calculated mechanical response. The statistical variation of properties is an intrinsic feature of the materials and as such should be considered in the analysis of their mechanical response. Further research works are needed to study this topic and determine to which extend a statistical variation of the properties is a prerequisite to a sound modelling of the mechanical behaviour of UHPFRC.
- Significant eigenstresses are induced in UHPFRC layers applied on concrete substrates. Their intensity depends to a large extent on the degree of restraint (by the substrate and by reinforcement bars) of the overlay. For the investigated cases, with a moderate to high degree of restraint, the eigenstresses never reach the tensile strength of the UHPFRC. Further research is needed to investigate the case of structural elements with a very high degree of restraint.
- The eigenstresses can explain the apparent “weak” tensile response of UHPFRC obtained in recent research works through inverse analysis of the fracture tests of composite structural members with UHPFRC.
- Sudden dimensional changes in the cross section of UHPFRC layers applied on concrete substrates induce significant stress concentrations.
- The models presented in this report can be combined to a later stage to study the interaction of eigenstresses and tensile fracture of UHPFRC in composite structural members at service state and ultimate limit state.





## 1. INTRODUCTION

The extremely low permeability of Ultra-High Performance Fibre Reinforced Concretes (UHPFRC) associated with their outstanding mechanical properties make them especially suitable to locally "harden" reinforced concrete structures in critical zones subjected to an aggressive environment and to significant mechanical stresses. UHPFRC materials can be applied on new structures, or on existing ones for rehabilitation, as thin watertight overlays in replacement of waterproofing membranes, as reinforcement layers combined with reinforcement bars, or as prefabricated elements such as kerbs, Figure 1.



**Figure 1:** Concept of application of UHPFRC for the rehabilitation of reinforced concrete structures.

The successful rehabilitation of existing structures is a **major challenge** for civil engineers. Indeed, design of reliable and durable concrete rehabilitations is often more complex than the design of a new structure. When existing concrete needs to be replaced, *a new composite structure* formed of the new material cast on the existing substrate will result from the intervention. Both the protective function and the mechanical performance of the composite system have to be guaranteed over the planned service life.

---

The numerical modelling of composite systems formed of cementitious materials of different ages has three main goals:

- determination of parameters and their evolution with time that are not accessible through experimentation (eigenstresses for instance),
- inverse analysis of experimental test results to determine fundamental properties (constitutive law in uniaxial tension, heat of hydration, diffusion coefficient, etc.),
- prediction of the response for different geometries and boundary conditions, parametric studies and design.

The numerical modelling of systems with multiple layers of cementitious materials with different ages requires comprehensive models of the time dependent behaviour at early-age and long term. UHPFRC require special consideration of their tensile hardening behaviour with significant bulk energy dissipation. Further, recent works, Habel (2004), have shown the significant influence of the softening part of the tensile behaviour of UHPFRC on the structural response of UHPFRC-concrete structural members. It is thus necessary for the application of these materials in composite construction to consider a global hardening- softening model for the UHPFRC.

Inverse analyses of fracture tests on composite UHPFRC-concrete members, performed with an analytical cross sectional model, with empirical characteristic length, Habel (2004), delivered uniaxial tensile laws completely different from the response measured in uniaxial tensile tests on notched specimens. This difference can be explained qualitatively by the use of notched specimens and effect of eigenstresses among others. It also reveals the need for in depth modelling of the tensile behaviour of UHPFRC by means of finite element simulations.

*The present report is devoted to the numerical modelling of (1) the mechanical response under quasi static tensile or flexural loading of UHPFRC and (2) the thermo-mechanical behaviour of a concrete member rehabilitated by means of an UHPFRC overlay.*

More specifically, the emphasis is put on the tensile behaviour of UHPFRC and the adequate modelling of their hardening-softening response by means of Finite Element codes (Smearred Crack Model).

First, a smeared crack model of the tensile behaviour of UHPFRC is validated and applied to the modelling of the fracture of UHPFRC under tensile loading, with different configurations (statistical variation of parameters and effect of the length of the specimen). Secondly, this model is applied to the inverse analysis of various bending tests with different types of UHPFRC. Finally, the time-dependent structural response of composite UHPFRC-concrete members (bi-material) with different geometries and degrees of restraint is determined in two different cases: UHPFRC overlay of uniform thickness and with an over depth.

## 2. MECHANICAL BEHAVIOR OF UHPFRC UNDER QUASI-STATIC UNIAXIAL TENSILE LOADING

### 2.1 Introduction

UHPFRC are characterised by a very low permeability and outstanding mechanical properties with respect to normal concretes. UHPFRC compressive strength can easily reach values exceeding 200 MPa at 28 days without any curing or treatment. Their Young's modulus is higher than that of conventional concretes. Its value ranges generally between 40 to 50 GPa at 28 days, roughly 10 to 30 % higher than other concretes. The Poisson's ratio for Reactive Powder Concrete (RPC) was determined to be 0.22 to 0.24, Dugat et al. (1996) and for CEMTEC<sub>multiscale</sub><sup>®</sup> to be 0.21 at 28 days, Parant (2003).

One of the main features of CEMTEC<sub>multiscale</sub> is its outstanding mechanical performance under tensile loading. Firstly, due to the very dense binding matrix (extremely low water/binder ratio and very fine particles) the material can reach much higher tensile strengths compared to conventional concretes (3 to 4 times more) and the addition of microfibers (steel wool) significantly increases the pseudo elastic domain. Secondly, the optimized multilevel fibrous reinforcement with short steel fibres confers to the material dramatically increased deformational and energy dissipation capabilities.

The uniaxial tensile behaviour of two different recipes of the UHPFRC CEMTEC<sub>multiscale</sub><sup>®</sup> type has been determined at 28 days, by means of a rigid fixed ends tensile test, Habel (2004) on unnotched dogbone specimens Denarié (2005). The average curves from five tests for each material are represented on Figure 2a, showing the range of possible strain hardening responses.

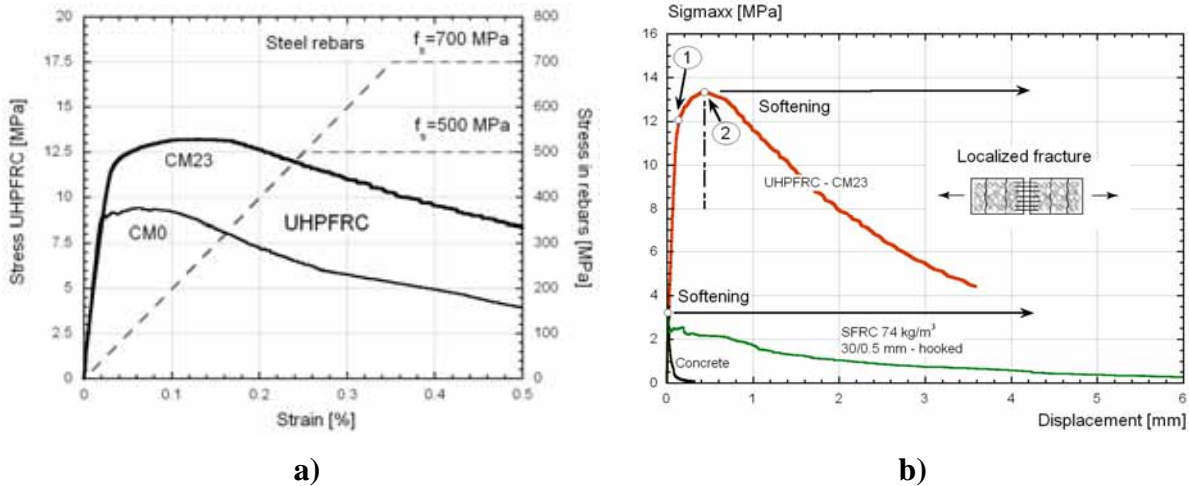
- Recipe CM0 is reinforced with a 468 kg/m<sup>3</sup> of a single type of 10 mm long steel fibres with an aspect ratio of 50. It has a water/binder ratio of 0.140, 1051 kg/m<sup>3</sup> cement, a fluid consistency (slump-flow = 700 mm) and is self-levelling.

- Recipe CM23 has more binder (1437 kg/m<sup>3</sup> cement) and a lower water-binder ratio (0.125). It is reinforced by a multilevel fibrous mix of macro steel fibres (10 mm long, aspect ratio 50) and microfibres (steel wool) with a total dosage of 705 kg/m<sup>3</sup>. The effect of the addition of microfibres is revealed by three aspects:

- (1) the significant increase of the pseudo-elastic domain from 8 to above 11 MPa.
- (2) the increase of the strain hardening domain.
- (3) the increase of the load carrying capacity in the descending branch due to the indirect action of the microfibres on the progressive pull-out of the macro fibres.

The tensile stress-strain curves of UHPFRC of the CEMTEC<sub>multiscale</sub> family exhibit a large strain-hardening response up to 0.2 %, in the range of the yield strain of ductile metals, as shown on Figure 2a.

The work of pull-out of the numerous fibres in the material explains the extremely high specific work of fracture of UHPFRC (up to 40'000 J/m<sup>2</sup> compared to 200 J/m<sup>2</sup> for normal concrete), as illustrated on Figure 2b.



**Figure 2:** : a) Tensile behaviour of two UHPFRC recipes, CEMTEC<sub>multiscale</sub>®, b)<sup>1</sup> comparison of tensile behaviour of UHPFRC CM23 with other materials.

The comparison between strain hardening HPFRCC<sup>2</sup> such as UHPFRC and conventional fibre reinforced concrete (FRC) is shown schematically in Figure 3, Naaman (2003). The stress-strain/displacement curves of both materials can be subdivided into three domains.

- *Domain I:* In the first part of the curves until point A, the stress rise is *quasi linear-elastic* until the cracking strength  $\sigma_{cc}$ ; in the following point B will refer to “peak”.
- *Domain II:* *Strain-hardening* until point B with a post-cracking strength  $\sigma_{pc}$  for UHPFRC. The post-cracking strength of UHPFRC is higher than the cracking strength.
- Multiple cracks form during the hardening phase, however, the macroscopic deformation is still uniform<sup>3</sup> and can be expressed by the strain  $\epsilon$ .<sup>4</sup>
- *Domain III:* At point B, *crack localization* occurs and softening behaviour is observed (domain III), expressed by a  $\sigma$ -w-curve.

<sup>1</sup> For the sake of simplicity and for comparison with metals, the deformation of the UHPFRC is represented in Figure 2a) by strains pre and post peak. However, the post-peak response should be characterized by displacements (crack openings). On another hand, the localization process in UHPFRC is a progressive process and is fully achieved significantly after the peak stress.

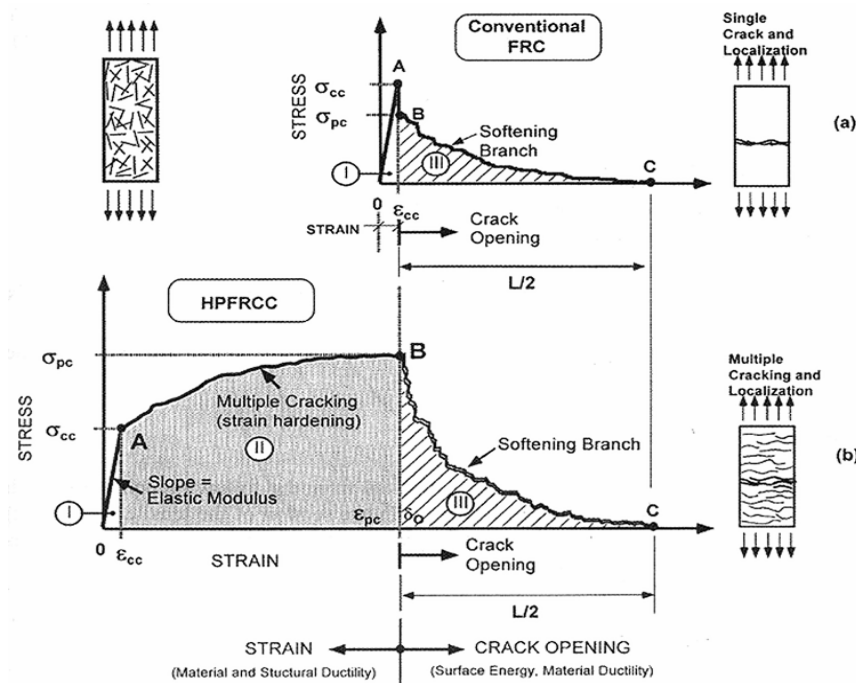
<sup>2</sup> UHPFRC and HPFRCC have both a significant tensile strain hardening response. UHPFRC is a subset of HPFRCC with a matrix with an extremely low permeability to liquids and gases.

<sup>3</sup> Macroscopic with respect to structural elements.

<sup>4</sup> The extent of the tensile hardening domain will be often referred in what follows as "Magnitude of Hardening - MH"



Domain II barely exists for conventional FRC. Typical maximum strengths of UHPFRC are 6 to 20 MPa with fracture energies of  $G_F = 10$  to  $40 \text{ kJ/m}^2$ , mainly dependent on the compactness of the matrix and fibre composition Dugat (1996), Parant (2003). Real cracks form (i.e. the stress becomes zero) for a crack width of approximately half the fibre length ( $\frac{1}{2} l_f$ ).



**Figure 3: Tensile behaviour of HPRC-UHPFRC and comparison with FRC and concrete, after Naaman (2003).**

## 2.2 Theoretical background

### 2.2.1 Materials with negligible volumetric energy dissipation

In case of conventional Fibre Reinforced Concrete, the applied fracture mechanics models are roughly the same as for quasi-brittle materials such as normal concrete. The reason for that is, for both materials, the A-C domain of the stress-strain curve (Figure 3) is nearly in-existent, in other terms the dissipated energy in this domain, due to an eventual volumetric inelasticity, is negligible compared to the energy dissipated in the post-peak part of the diagram (Point B to C in Figure 3). The descending branch B-C of the stress displacement curve is referred as “softening branch” and governs the formation and development of the surfacic fracturing process. During this phase the energy is totally dissipated in a localized band of multiple microcracks which will degenerate into a real macrocrack. It must be outlined that this energy, called fracture energy ( $G_F$ ) is related to the area of the main *surface* of the crack band (macrocrack) and not to the entire *volume* of the specimen. In other terms, it is pure *surfacic* energy dissipation. For these softening materials, many well-established approaches and

---

models exist since a long time and have been successfully applied in different fields of civil engineering and material sciences. The two most used models, called “cohesive crack-models”, implemented in many FE-Codes (MLS, MERLIN, DIANA, ATENA; MARC, ABAQUS, among others) are:

1) The “Fictitious Crack Model” (FCM), Hillerborg (1983), the crack is represented by a discrete plane, as an interfacial element between two plain finite elements, in which the fracture energy is totally dissipated. *The major advantage of the FCM is its mesh insensitivity. The major disadvantage is the need either to predetermine the crack paths or to perform remeshing after each crack propagation.*

2) The “Crack Band Model” (CBM), Bazant et Oh (1983), representing fracture in a smeared manner. In this approach, microcracks of infinitely small opening are supposed to be continuously distributed (smeared) over a finite band of finite elements. This is generally modelled by gradually reducing the stiffness and the tensile strength in the direction normal to the crack after the peak strength has been reached. Mesh size independency is achieved by scaling the  $\sigma$ - $w$  softening law on the basis of the mesh size to obtain the  $\sigma$ - $\varepsilon$  law used in the calculations, with the objective to conserve the specific fracture energy  $G_F$ .

*The major advantage of this model is its general applicability without needing to predetermine the crack path. The major drawback is the mesh sensitivity which has to be compensated by appropriate normalization of the constitutive softening law with respect to finite element sizes.*

In both models crack initiates once the tensile stress reaches the tensile strength of the material ( $\sigma_{cc}$  in Figure 3). The evolution of the cracking process down to full fracture is governed by the stress-crack opening law of the material (B-C in Figure 3). For normal concrete and conventional FRC, the softening response is often idealized by a multi-linear diagram or by a decreasing exponential curve.

These models are largely described in literature and their FE implementation in the user manuals of the above mentioned FE-Codes.

## **2.2.2 Materials with volumetric and surfacic energy dissipation**

In UHPFRC under tensile loading (and more generally speaking in all materials with significant bulk dissipation such as HPRCC), energy dissipation is not only related to one cross-section or localized area of the specimen but also to the entire *volume* of the specimen.

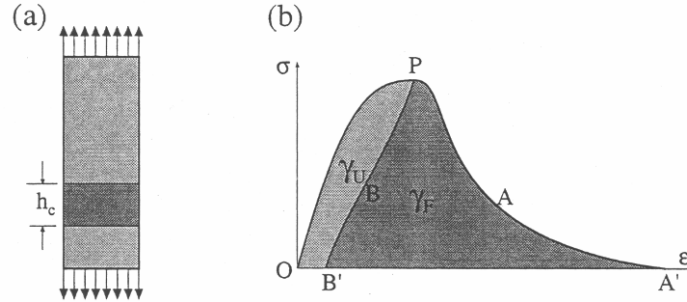
Tailhan (2003), cited by Parant (2003), applied an elastoplastic model to characterize the tensile response of the UHPFRC CEMTEC<sub>multiscale</sub>®. The model, limited to the prepeak range, was able to represent accurately the flexural response of UHPFRC plates, prepeak, up to the peak force experimentally determined by Parant (2003).

For the modelling of composite structural members with low strain gradients in the UHPFRC, softening of the UHPFRC plays a significant role even in the prepeak range. It is thus necessary to consider tensile models with combined hardening-softening behaviour. However, the smeared crack model has to be adapted to properly model both components of the energy dissipation and preserve mesh size independency.. This is done according to the principles set forth by Bazant and Oh (2003), as shown on Figure 4 from Bazant & Planas (1998).

A specimen with length  $L$  and cross section  $A$ , is subjected to direct tension. The fracture localizes in a zone of finite width  $h_c$ . The total work of fracture  $W_F$  is composed of the surfacic

and volumetric contributions, equation (1), with  $\gamma_F$  = Specific surfacic fracture energy divided by the band width  $h_c$  ( $J/m^3$ ) over which the localized fracture is smeared, and  $\gamma_u$  specific volumetric fracture energy, dissipated over the whole length of the specimen, L..

$$W_F = G_F A + G_v V = Ah_c \gamma_F + AL \gamma_u \quad (1)$$



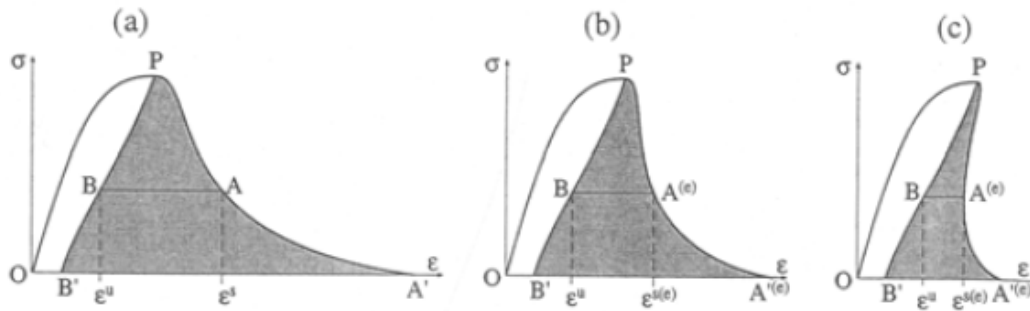
**Figure 4: Crack band model of Bazant and Oh (1983), generalization to materials with significant bulk dissipation, Bazant and Planas (1998).**

- The volumic part of dissipation (hardening domain – pre-peak) is defined on the basis of a uniaxial tensile test ( $\sigma$ -w diagram) in which the displacement w is normalized by a characteristic length  $h(e)$ <sup>5</sup> independent of the mesh size.  $h(e)$  is usually the measurement basis of the transducers on the representative volume<sup>6</sup>, in a uniaxial tensile test.
- The surfacic part of dissipation is given by the softening part of the constitutive law defined on the basis of a  $\sigma$ -w diagram, such as *the surfacic dissipation  $G_F$  is conserved between the constitutive law and in the finite elements*. This condition imposes a scaling of the softening branch according to the ratio between the characteristic length of the mesh  $h_c$  and the characteristic length  $h(e)$  associated to the testing procedure of the material, equation (2), Bazant and Planas (1998), as illustrated on Figure 5.

$$\epsilon^{s(e)} - \epsilon^u = \frac{h_c}{h(e)} (\epsilon^{s(e)} - \epsilon^u) \quad (2)$$

<sup>5</sup> In the following chapters of the document,, the volumetric characteristic length will be referred as Lvol.

<sup>6</sup> The representative volume is meant for the onset and development of the strain hardening response. This volume should enable the development of multiple cracks, with a constant cross section and no notch.



**Figure 5: Constitutive tensile law for a finite element of size  $h_c$ , c) snapback effect of the scaling of the softening branch, due to oversized finite element.**

The smeared crack model already existing in Software MLS, from FEMMASSE b.v. Roelfstra et al. (1994, has been modified according to equation (2) to consider the effect of bulk energy dissipation.

## 2.3 Modelling of the tensile behaviour of UHPFRC with MLS-software

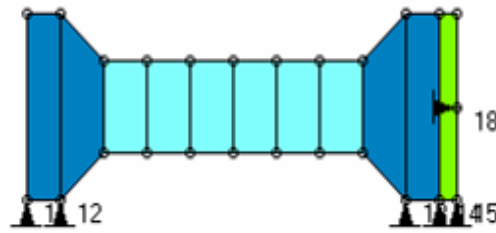
### 2.3.1 Scopes

In this chapter, the smeared crack model for the tensile behaviour of UHPFRC is validated and applied to different cases:

- Test of mesh size independency
- Influence of statistical distribution of the stress-strain hardening-softening parameters
- Influence of the length of the tensile specimen on the apparent response under tension.

### 2.3.2 Influence of the FE-size

The influence of the finite element (FE) size on the mechanical response in a tensile test is tested on a dogbone specimen geometry used for tensile tests. An increasing displacement is imposed at the end face of the specimen. The length and the width of the specimen are 300 (central part with constant width) and 100 mm respectively, with a unit thickness. The specimen is first subdivided in contiguous macro-element as shown in Figure 6 . The same figure shows schematically the location of the supports and the loading point (point “18” in the figure).

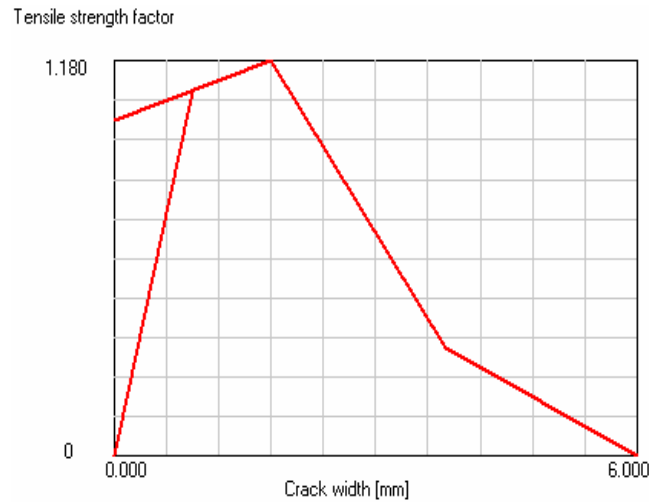


**Figure 6: Schematic representation of the dogbone-shaped specimen, its subdivision in macro-elements, supports and loading point, as given by the graphical pre-processor of MLS.**

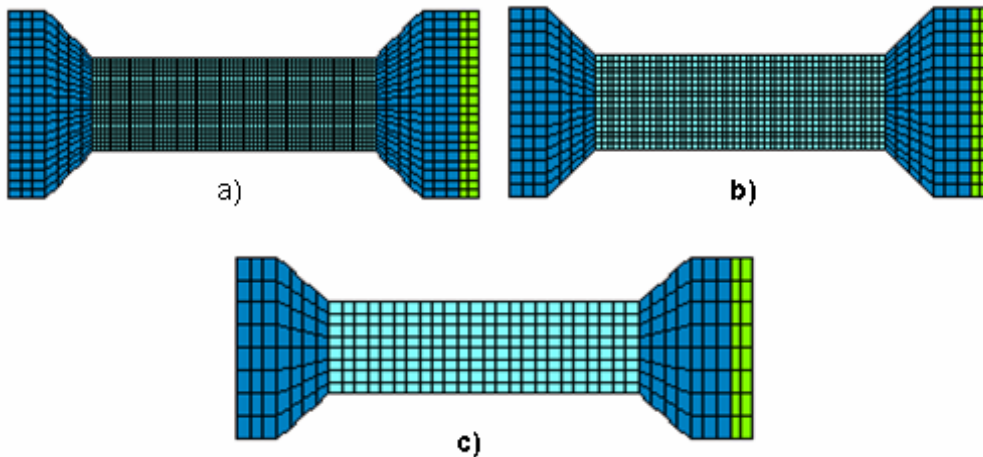
The macro-elements representing the end-parts of the dogbone specimen are assumed to behave in a linear elastic manner, with a Young's modulus and a Poisson's ratio of 50GPa and 0.2, respectively. A stiff steel plate is applied at the right end-face of the specimen to keep a uniform distribution of nodal displacements on this face while a nodal displacement is applied at point 18..

The constitutive tensile behaviour of the macro-elements in the central part of the specimen, with a constant width, is given by a stress-strain hardening-softening diagram shown in Figure 7. The tensile strength factor is the ratio of the strength for a given displacement, to the first crack strength (11 MPa). Young's modulus and Poisson's ratio are the same as for macro-elements representing the end parts in UHPFRC. The tensile strength ( $f_t$  or  $\sigma_{cc}$ ) and characteristic length for the volumetric dissipation ( $L_{vol}$ ) are 11 MPa and 430 mm, respectively. The macro-elements are then subdivided into finer FE. The subdivision in macro-elements allows the user to introduce at a later stage, if required, interfacial elements between adjacent macro-elements. Different mesh refinements of the macro-elements are considered to assess the influence of the FE-size on the mechanical response of the system. Figure 8 shows three FE idealizations of the dogbone-shaped test specimen with a gradual increase of the FE-size, (a) 5 mm, (b) 10 mm and (c) 20mm.

Figure 9 shows distribution of damage induced during the strain hardening phase for the three models and at four different load levels, corresponding to following imposed displacements: (a) 1.30, (b) 1.40, (c) 2.00 and (d) 4.00 mm. First of all, we can notice that damage induced during the hardening phase starts in the angular regions of the specimen, independently on the FE-size. This effect is attributed to the presence of the angles which play a role of stress concentrators. Tensile stresses in these regions reach quicker the tensile strength ( $f_t$  or  $\sigma_{cc}$ ) of the material then they do in the remaining volume. The hardening-induced damage becomes more and more intense and simultaneously propagates further towards the centre of the specimen. It must be outlined that in case of the model with the finest FE mesh, hardening-induced damage is confined in the near end-face zones, while the central zone remains undamaged, even at the final rupture of the specimen. In models with larger FE-size, the hardening phase of the specimen is active in almost the entire volume of the specimen.



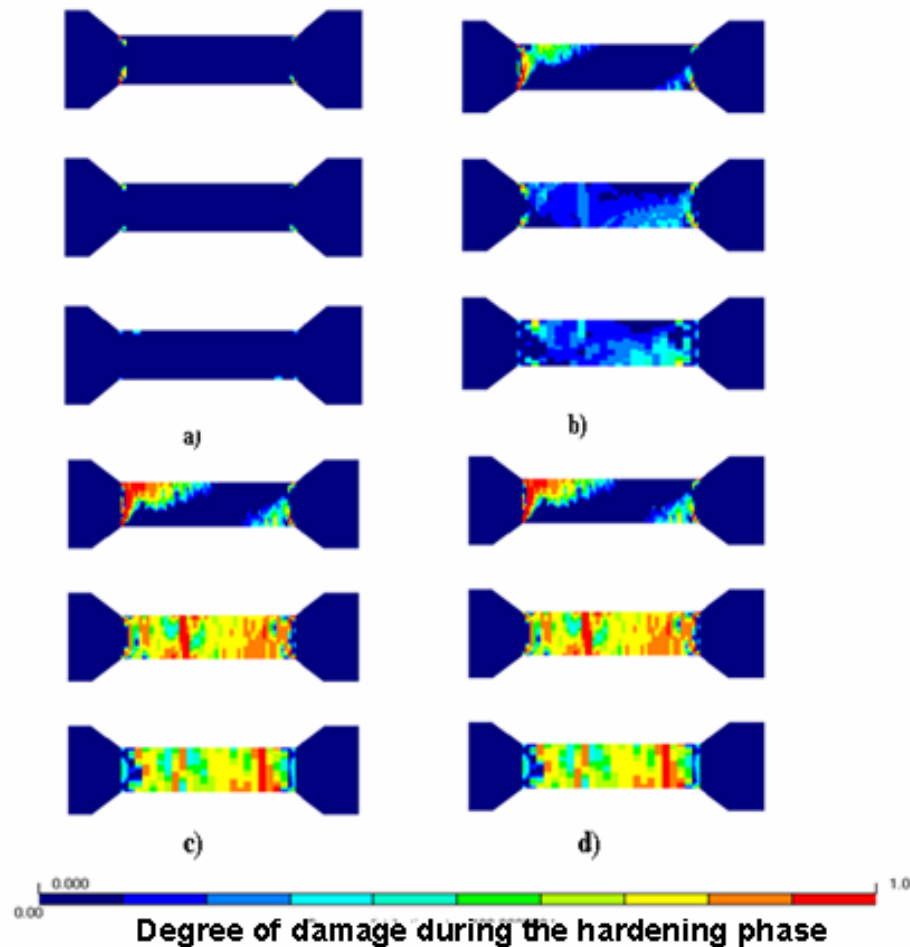
**Figure 7:** Stress-strain hardening-softening of the material as introduced and visualized in MLS-FE Code, the stresses are normalized to the tensile strength ( $\sigma_{cc}$ ) ( $L_{vol}$ : 430mm).



**Figure 8:** FE-idealizations of the dogbone-shaped tensile test specimens with three different FE-sizes: a) 5, b) 10 and c) 20 mm.

The reason is that in the finest idealization, a macro-crack (band of smeared microcracks) starts to form earlier (in terms of imposed load-level), meaning that the softening phase of the material is already activated and governs the further mechanical behaviour of the specimen. From this stage, the mean value of the tensile stress in the system decreases accordingly to the stress-strain softening law, as a consequence, the remaining sound FE can not any more reach the hardening phase, but rather they unload linear-elastically. According to these numerical findings, it can be concluded that, as soon as a microcracked band starts to build up, any further supplied external energy is totally dissipated by an ongoing development of fracturing (softening regime) of the microcracked zone which finally degenerate to a real crack. This conclusion can be drawn under the condition that the material is purely homogenous. As we will see later, this “competition” between hardening and softening processes acts differently if

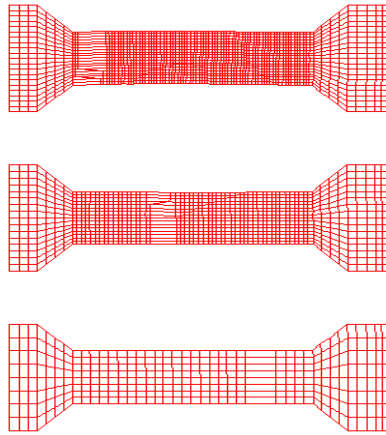
the mechanical parameters of the material, such as the tensile strength, are considered as a statistical variable.



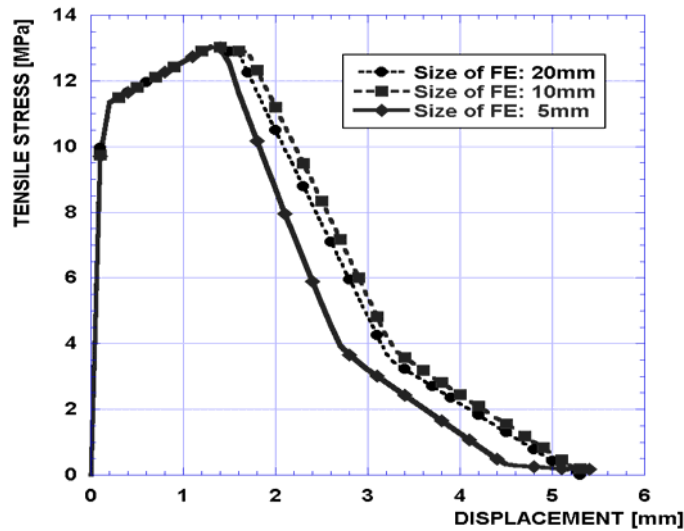
**Figure 9:** Evolution of damage distribution in the specimens at 4 increasing load-levels: a) 1.30, b) 1.40, c) 2.00 and d) 4.00 mm.

At a load level of roughly 1.6 mm (imposed displacement), equivalent to 0.37 % strain over a basis of 430 mm, a well localized microcracked band is formed. From this stage, the deterioration process is predominantly governed by the softening regime of the microcracked zone, which will finally degenerate into a real crack. As it can be seen in Figure 9-c and d, damage distribution remains almost the same between load levels: 2 and 4 mm. All energy is then dissipated by a progressive widening of the already well formed and localised microcracked band.

Figure 10 shows deformed shapes of the specimens at a load-level of 2mm. The microcracked bands are clearly visible. Two remarks can be made: firstly, for all models one microcracked band only is formed, secondly, the localisation of this band differs from a model to the other. In other words, the localisation of the crack seems to be mesh-dependent. This can be attributed to the different operations involved at each step in the computation process (incremental loading steps, accumulation of round off errors, etc). This point has to be checked in further work.



**Figure 10:** Deformed shapes showing the widening of the microcracked band at an advanced load level (2 mm).



**Figure 11:** Simulated stress-deformation responses for the model with three different mesh refinements.

Figure 11 shows the simulated stress-displacement curves obtained for the three different meshes. One can see that, independently of the FE-size, that the MLS numerical results reflect the introduced (input) stress-strain hardening-softening law of the material. The small dependency on the size of FE is quite acceptable and probably unavoidable in FE-codes. Further, the modelling of a given specimen introduces a structural component that unavoidably slightly deviates the calculated response from the input laws.



### 2.3.3 Influence of a statistical variation of the strength

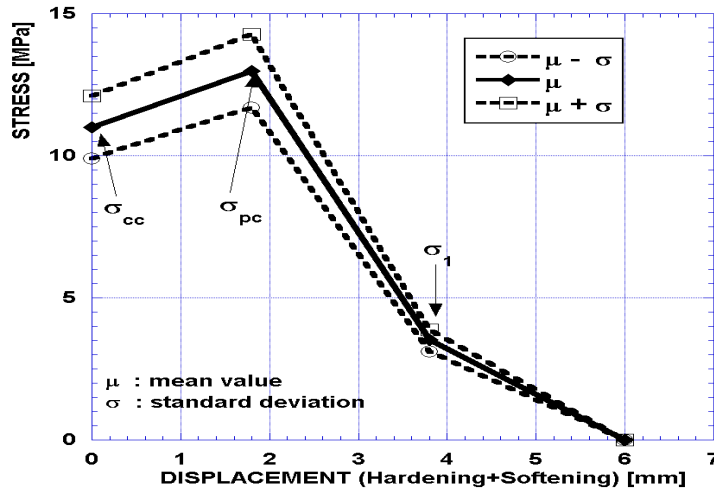
It is well known that the micro and/or mesoscopic structure of granular materials, such as cement-based materials, with or without fibre reinforcements, is never homogenous. The heterogeneous character of the structure leads inevitably to a scatter of the material parameters. The heterogeneous nature of the material in analyses at the macro level can be taken into account by material parameters defined as statistical variables following given distribution functions with a distribution function (Gauss, Weibull, for instance) and mean value and standard deviation.

*In this section we will focus the study on the scatter of the tensile strengths of the stress-strain hardening-softening diagram, by means of model implemented in MLS-code to define tensile parameters as statistical variables.*

In MLS, tensile strengths are randomly distributed in FE according to a Gauss' function defined by their mean values and their corresponding standard deviation. Unfortunately no realistic correlation between statistical distributions of the different tensile strengths of the stress-strain hardening-softening law can be introduced. MLS assumes that all strength distribution functions are identical. Meaning that if in a given FE  $\sigma_{cc}$  is  $x$  % lower or higher than its mean value, the other strengths ( $\sigma_{cp}$ ,  $\sigma_1$ , etc..., see definition in Figure 3) of the same FE are also varied by a similar percentage of their mean values. The way adopted by MLS for the distributions of strengths is explained schematically in Figure 12. In this figure, the tensile behaviour of the material is described by a linear strain-hardening domain followed by a bilinear strain-softening domain. The adopted correlation between statistical distributions of the different tensile strengths of the stress-strain law of the material is not realistic because the tensile strength (in our case  $\sigma_{cc}$ ) is defined by the microstructure of the binding matrix while the remaining strengths ( $\sigma_{cp}$ ,  $\sigma_1$ ,...) are strongly dependent not only on the fibre content but also on the geometrical (dimensions, orientation, etc...) and mechanical (stiffness, resistance, roughness of the surface, etc...) characteristics of the fibres.

In the following numerical simulations the stress-strain hardening-softening of the material shown in Figure 12 is considered. Tensile strengths ( $\sigma_{cc}$ ,  $\sigma_{cp}$ ,  $\sigma_1$ ) are normally distributed with the following respective mean values, 11.00, 12.98 and 3.52 MPa (this realistic material law was deduced from an experimental curve by an inverse analysis). The standard deviations are chosen to be equal to 10% of the mean value of the strengths and a cut-off (lower and upper limit values) of the Gauss distribution function at one unit of the standard deviation is assumed. This statistical analysis is combined with the influence of the FE size.

The three FE meshes shown in Figure 6 are used in the following. The simulated stress-displacement responses are given in Figure 13 and compared to the results obtained for constant material parameters (homogeneous material). To outline the influence of statistically distributed tensile strengths on the evolution of the hardening-induced damage, Figure 14 give a comparison between the homogeneous and the statistical models for two load levels.



**Figure 12:** Example of statistical variation of the stress-strain hardening softening law, the solid diagram represents the mean curve( $\mu$ ) and dashed diagrams are curves with lowest value ( $\mu - \sigma$ ) and highest value ( $\mu + \sigma$ ), ( $\mu$  and  $\sigma$  are the mean value of the tensile strength and the standard deviation).

In all FE-meshes, the hardening process initiates much earlier in case of statistically distributed tensile strengths than in the homogeneous one. This due to the fact that in case of statistically distributed parameters, 50% of FE in the specimens underlie tensile strength ( $\sigma_{cc}$ ) lower than the mean value (11 MPa). Meaning that the criterion of the transition from linear elastic regime to the hardening phase ( $\sigma > \sigma_{cc}$ ) is quicker (in terms of increasing displacement) reached than in case of constant strength ( $\sigma_{cc}$ ).

As it can be seen in Figure 14a and b, in the case with constant parameters and for a load level of roughly 1.3 mm; FE activate in the hardening phase are mostly localized near the corners of the specimens and with a low degree of damage (Figure 14a). In case of statistically distributed strengths (see Figure 14b), the development of damage in hardening phase is totally different. The degree and the volume (surface in our case (2D analyses)) of hardening-induced damage are much higher (orange and red colours in pictures) and the damaged finite elements are “randomly” dispersed in the whole specimens. As the load further increases, hardening-induced damage distribution in the specimen remains roughly the same but it slightly increases in severity. In other terms, no further zones (finite elements) are subjected to the hardening process, they remain in linear elastic regime (see Figure 14b and d).

In the case of constant parameters, the number of zones (FE) in hardening phase increases slowly as the displacement increases. At an advanced load level, almost the whole volume of the specimen is swamped by hardening-induced damage, apart the finest mesh.

As consequences, in the case of statistically distributed strengths, the volume in hardening phase is clearly smaller than in the case of constant parameters. This obviously reflected in the resulting stress-displacement curves shown in Figure 13. This effect is unfortunately unfavourable in practice, because only a reduced part of the deformability potential of the material is used.

The earlier arise of the microcracked band(s) in the case of statistically distributed strength is also reflected in the response curves shown in Figure 13.

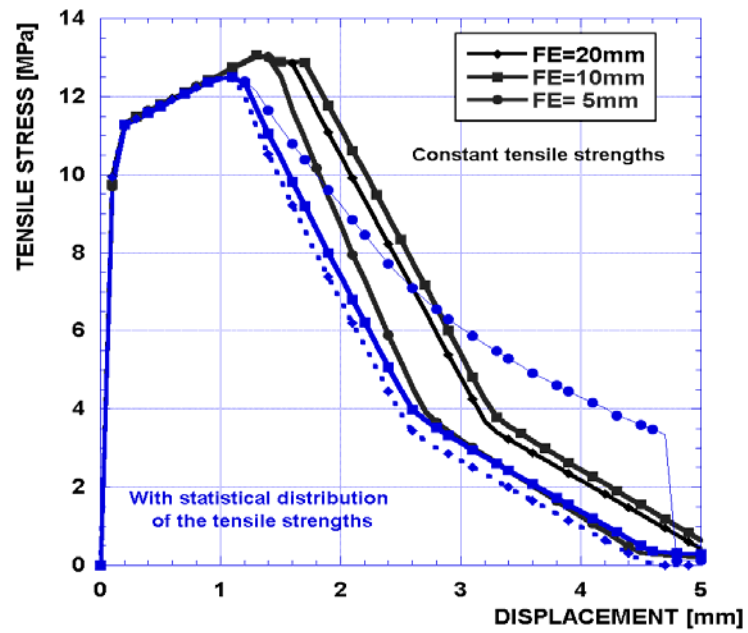
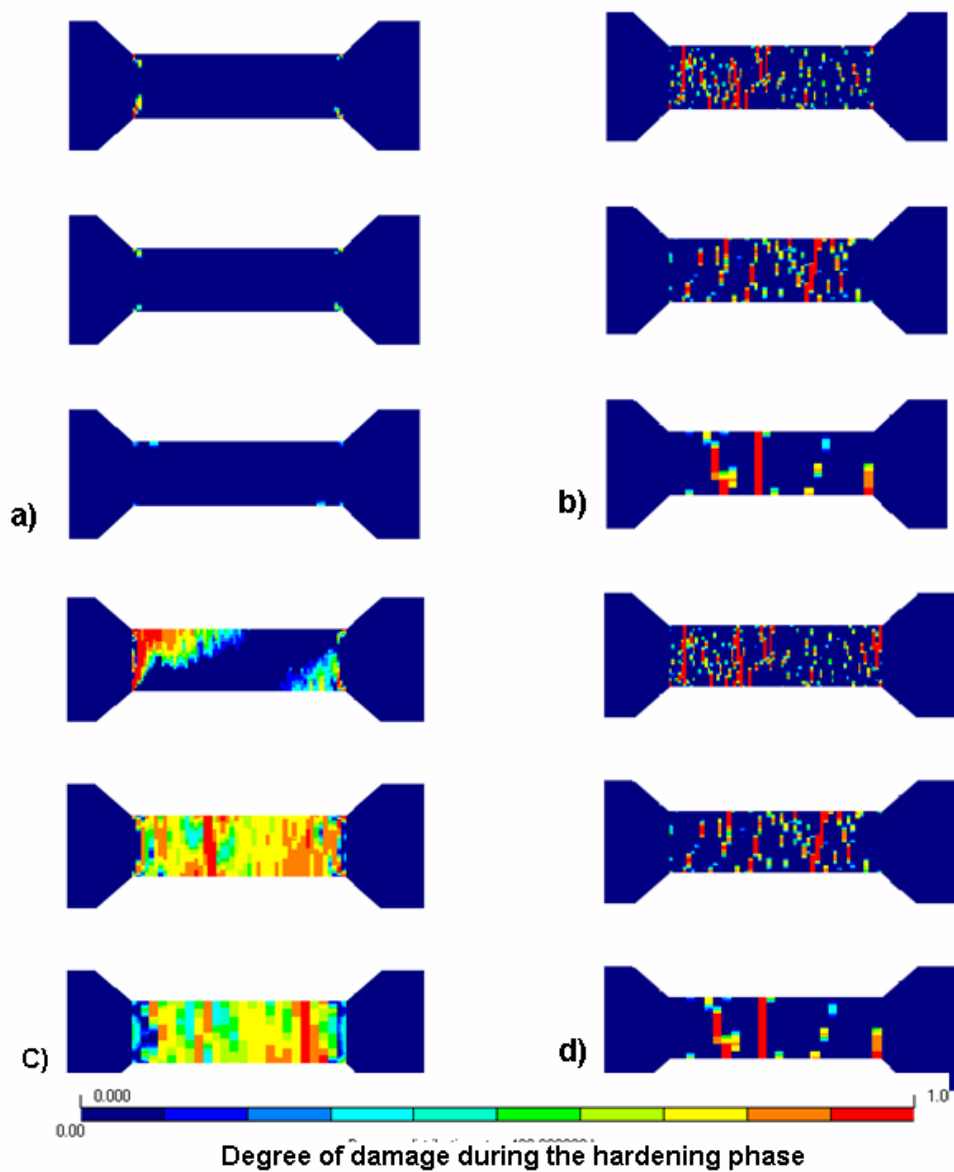
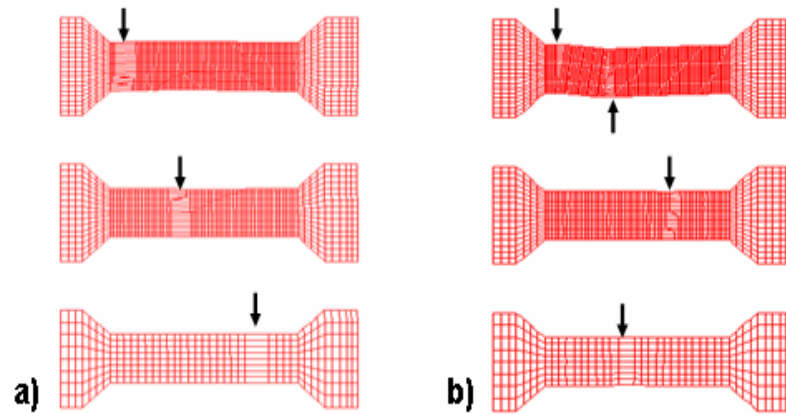


Figure 13: Comparison between simulated response of the dogbone-shaped test specimens with and without statistical distribution of the hardening and softening tensile strengths.



**Figure 14:** Comparison of damage distribution and evolution during hardening phase for the case with constant material parameters (left, a and c) and for the case with statistically distributed tensile strengths (right, b and d) at two different load-levels: 1.3 mm (a and b) and 4 mm (c and d).



**Figure 15: Localisation of microcracked bands (real cracks, shown by arrows) in the specimens at an imposed displacement of 2mm, (a) homogeneous, (b) statistically distributed tensile strengths.**

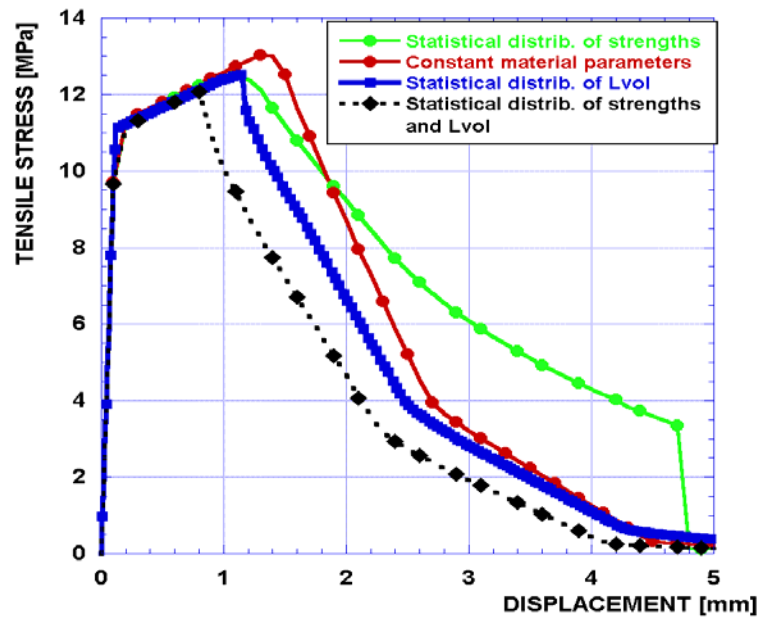
### 2.3.4 Combined influences of statistical distribution of tensile strength and extend of the hardening domain

Statistical distribution of the tensile strength of conventional cement-based material are well established, documented and often used in numerical simulation particularly for crack localisation. Tensile behaviour of UHPFRCC is not only dependent on its tensile resistance but also on the so-called magnitude of the hardening which is an intrinsic parameter of these materials. It depends on the geometrical and mechanical properties of the fibres and on their bond with the binding matrix. Until now, scarce information is available concerning the variability of the extend of the tensile hardening domain on a statistical basis. Despite this lack of knowledge, it is important to evaluate by means of finite elements the influence of this parameter on the tensile response. Thus this effect was implemented in MLS-Code as a statistical variation of the volumetric characteristic length  $L_{vol}$ , distributed according to a Gaussian function. The following numerical simulations have been performed and compared:

1. Statistical distribution of the tensile strengths of  $(\sigma_{cc}, \sigma_{cp}, \sigma_1)$
2. Statistical distribution of  $L_{vol}$
3. Statistical distribution of both tensile strengths of  $(\sigma_{cc}, \sigma_{cp}, \sigma_1)$  and  $L_{vol}$

The resulting stress-displacement curves are given in Figure 16 and compared to the case of an homogenous material. We can conclude that in all statistical models (1,2 and 3) the introduction of variability on a material parameter leads to a lower effective magnitude of the hardening domain and a lower effective tensile strength ( initiation of real crack,  $\sigma_{cp}$  in Figure 3) than in the case of a homogenous material.

*These results seem to be logical, but we think that is too early to draw faithful conclusions because of the lake of our knowledge, as mentioned above. Deeper experimental, numerical and analytical investigations must be carried out in this field.*



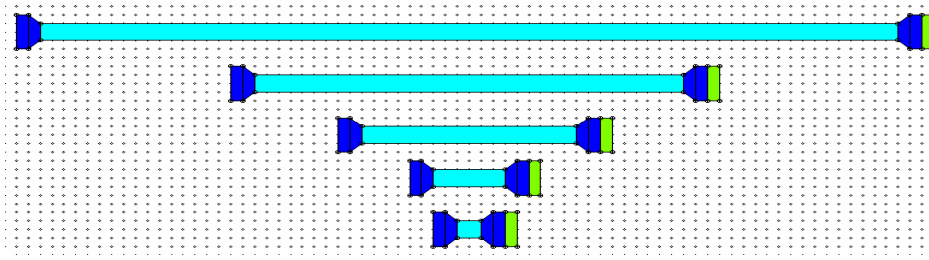
**Figure 16:** Comparison of the tensile behaviour by using different statistical distributions of the parameters of the stress-strain hardening-softening law (tensile strengths and characteristic hardening volume length (Lvol)).

### 2.3.5 Influence of the length of the tensile specimen on the mechanical response (size effect)

In order to study the influence of the length of the tensile specimen (size effect) on the macroscopic response of the system, the following numerical simulation has been carried out by using MLS-code. Uniaxial tensile dogbone-shaped specimens with increasing lengths from 100 to 3600 mm have been considered. The geometrical configuration is shown in Figure 17. In all specimens, the finite elements are squares with a side of 25mm. The specimens are simultaneously loaded by imposing the same incremental displacement function.

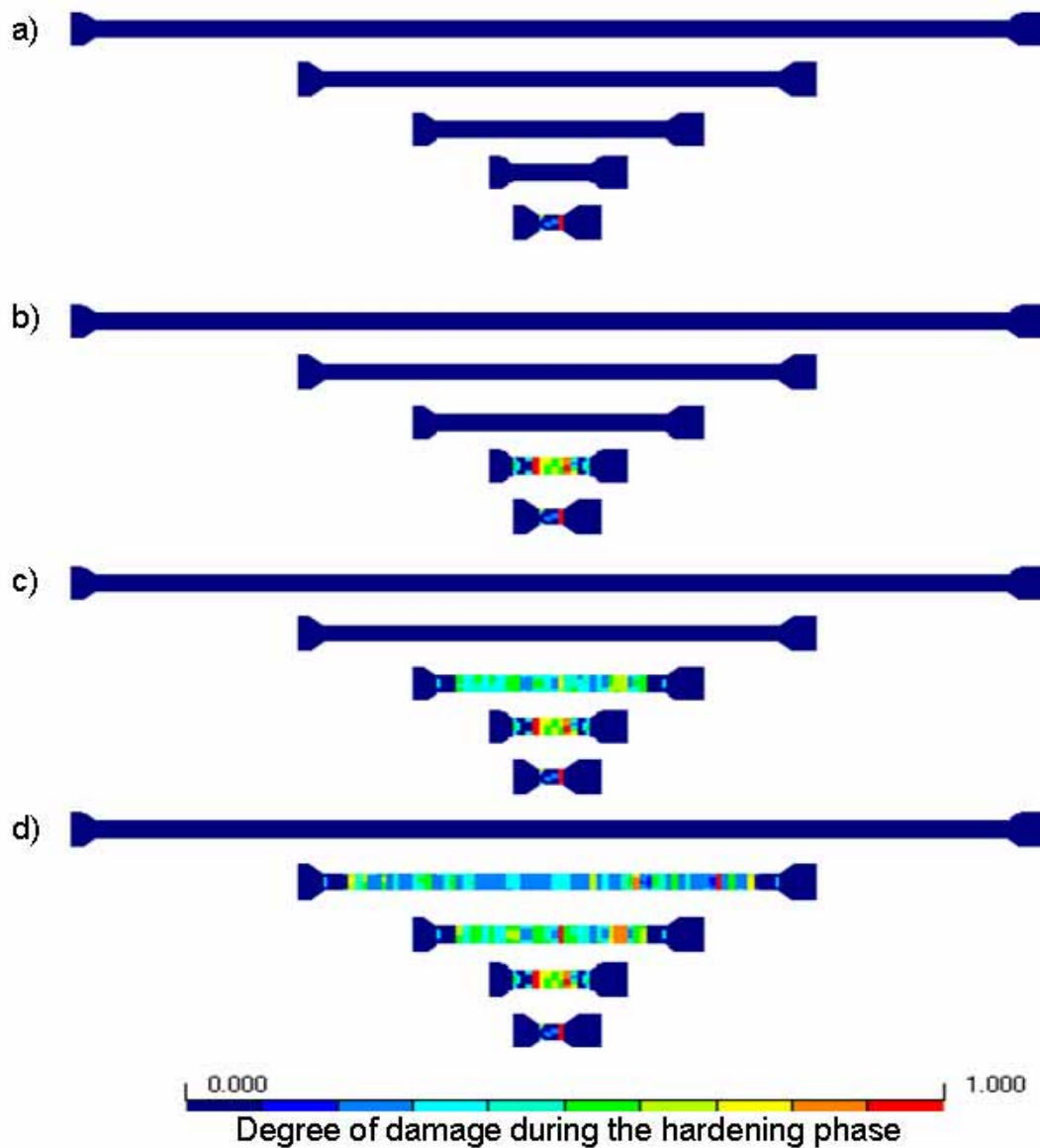
Figure 18a, b, c and d show the evolution of the distribution of damage during hardening phase in all specimens at 4 imposed displacement-levels, namely, 0.6, 2, 4 and 6 mm. As it can be seen, damage appears progressively in specimens, starting from the shortest one to the largest one, proportionally to the length of the specimen. Damage initiates as soon as the system leaves the linear-elastic regime. The resulting load displacement curves are shown in Figure 19. The peak strength ( $\sigma_{cp}$  in Figure 3) is roughly the same, independently of the length of specimen, except for the longest one which fails down brutally at a displacement level of roughly 10 mm (no control was any more possible).

In the following, due to the encountered instability, the longest specimen is kept apart from the interpretation of the numerical results. The softening branch and the corresponding fracture energy ( $G_f$ ) dissipated by the formation and the development of the crack (microcracked band) down to full fracture of the specimen is deduced from the stress-load curves shown in Figure 19 (descending branch of the curves). Figure 20 shows the deduced softening behaviour in terms of stress as function of crack opening displacement (COD). For the three shortest



**Figure 17: Dogbone tensile test specimens with increasing lengths: 100, 300, 900, 1800 and 3600mm, from down to up, respectively. Thickness constant (100mm)**

specimens, the *shape of the softening curve* is roughly the same; while the specimen with a length of 1800 mm (curve (4) in the figure) is slightly different. Its behaviour is a little bit less ductile than the other, probably instability effect starts progressively from this length value (i.e. the specimen with a length of 3600mm was instable, see Figure 19). Fracture energy ( $G_f$ ), represented by the area lying under the stress-strain softening curve is given in Figure 21 as function of the length of the specimen.  $G_f$  decreases slightly as length of the specimen increases. In the same figure, the magnitude of the hardening domain (MH) is plotted as function of the length of the specimen. The MH increases linearly with the length of the specimen, meaning that the energy dissipated during the hardening phase per unit volume is independent of the length of the specimen. The result seems to be obvious, because in the performed analysis all finite elements have the same properties (the material is assumed to be homogeneous). As we will see briefly later, if the material is assumed to be heterogeneous, the former drawn assertion is not any more valid.



**Figure 18:** Evolution of damage induced during the hardening phase in the 5 dogbone-shaped tensile test specimens during the hardening phase at four displacement levels: (a) 0.6, (b) 2, (c) 4 and (d) 6mm.



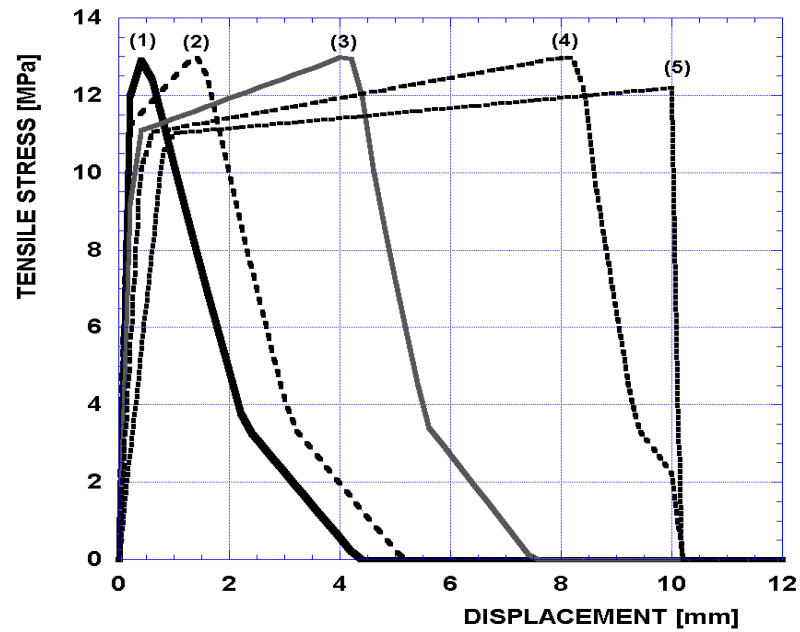


Figure 19: Simulated stress-displacement curves for dogbone-shaped tensile specimens with different lengths (1): 100mm, (2): 300mm, (3): 900mm; (4): 1800mm and (5): 3600mm.

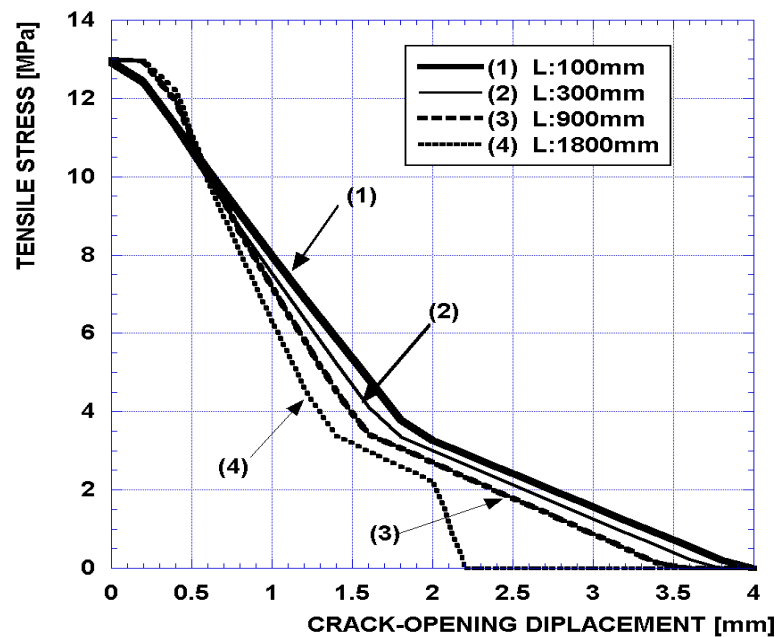


Figure 20: Stress Crack Opening Displacement (COD) as function of the specimen length deduced from the simulated stress-displacement curves shown in Figure 19.

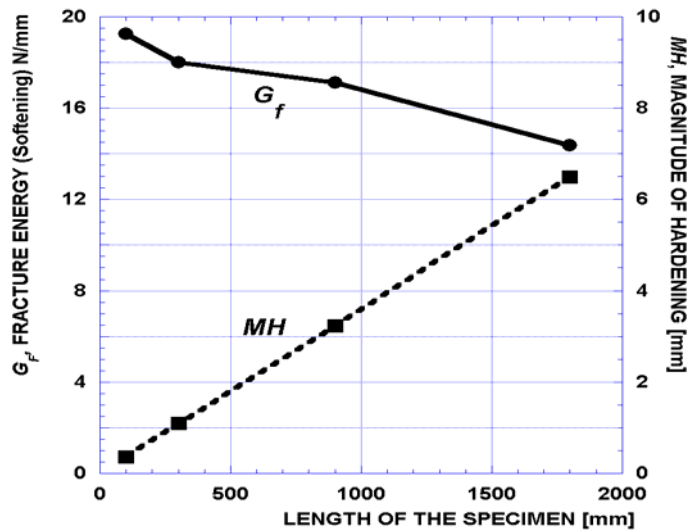


Figure 21: Fracture energy ( $G_F$ ) and magnitude of hardening (MH) as function of the length of the specimen.

### 2.3.6 Influence of combined statistically distributed strengths and length of the specimen

The above used model composed on dogbone-shaped tensile specimens (see Figure 17) with increasing length has been considered to study the influence of statistically distributed strengths. The specimen with the largest length (3600mm) is omitted in the comparison with the homogeneous model, because of its brutal rupture (instability), (see Figure 19).

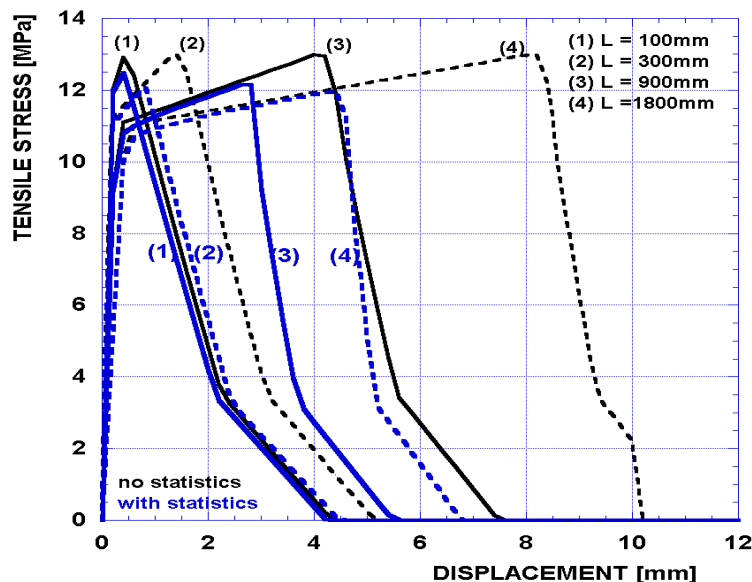
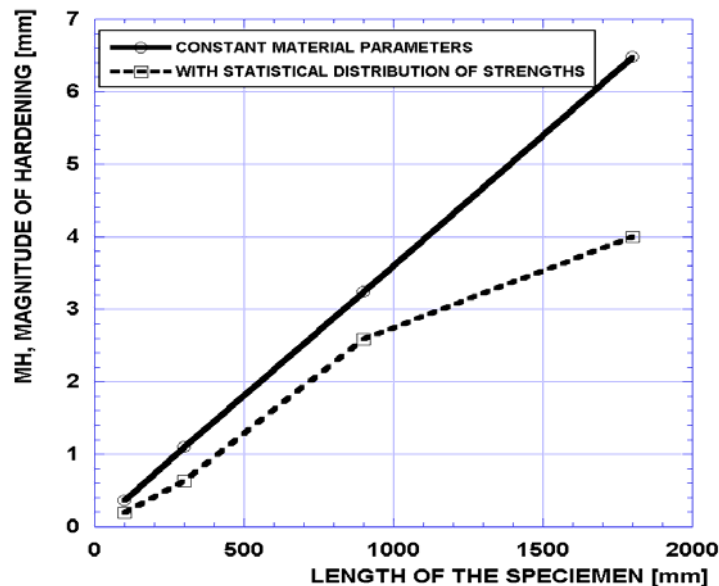


Figure 22: Comparison of the simulated stress-displacement curves between the case of a homogeneous material (black curves) and the case of statistically distributed tensile strengths (blue curves).

Figure 22 shows the comparison of the simulated load-displacement curves between the model with constant material parameters and the model with statistically distributed tensile strengths. A first analysis of this figure leads to the following remarks:

- For all specimen lengths, the maximum stress (peak load) is lower in the case of statistically distributed tensile strengths than in the homogenous model.
- In the model with statistically distributed tensile strengths, the peak load decreases as the length of the specimen increases, while it remains quasi-constant in the other model.
- For a given specimen length, the magnitude of the hardening domain (MH) is lower in case of statistically distributed tensile strengths. The MH as function of the specimen length is shown in Figure 23 and compared to the results of the model with constant parameters. In case of the statistical model, the relationship between the MH and the length of the specimen is still an increasing function, but not any more linear. For the longest specimen ( $L=1800\text{mm}$ ), the MH is approximately 60% lower than in specimen of constant material parameters.
- As it has been shown if the global shape of the post-peak behaviour (softening regime) is roughly the same for the both models, however, the resulting fracture energy ( $G_f$ ) is:
  - For a given specimen length, lower in case of statistical model
  - In case of the statistical model,  $G_f$  decreases strongly with the increasing length of the specimen. This decrease is less pronounced in the other model as it can be shown in Figure 25.



**Figure 23:** Magnitude of the hardening domain as function of the length of the specimen for a homogeneous material and for a material with statistically distributed tensile strengths.

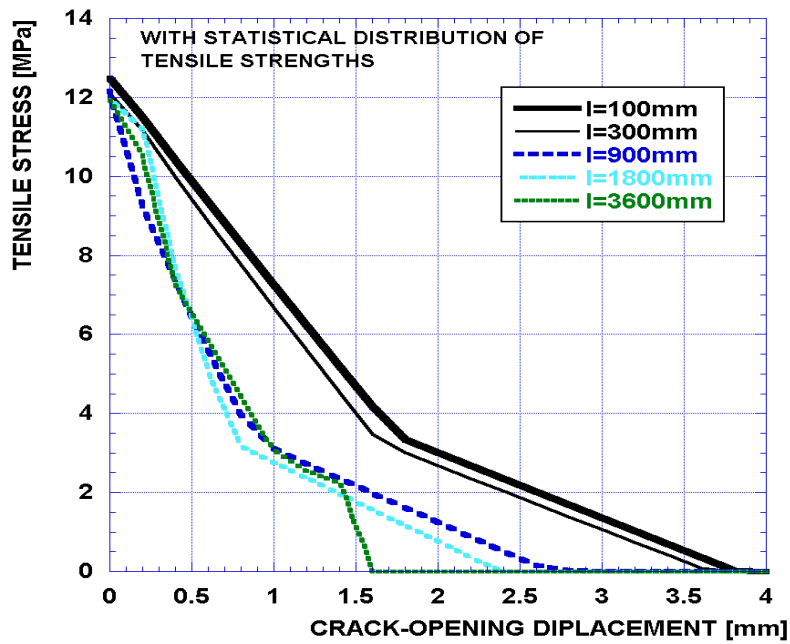


Figure 24: Deduced stress-crack opening displacement (COD) diagrams, (softening regime)

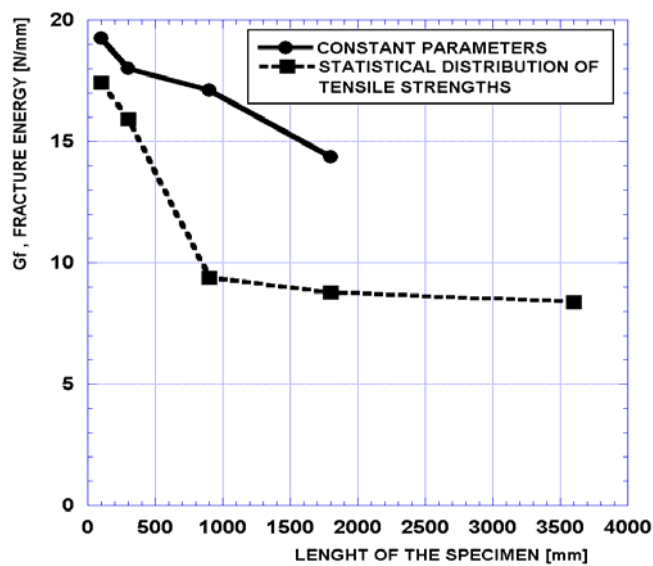
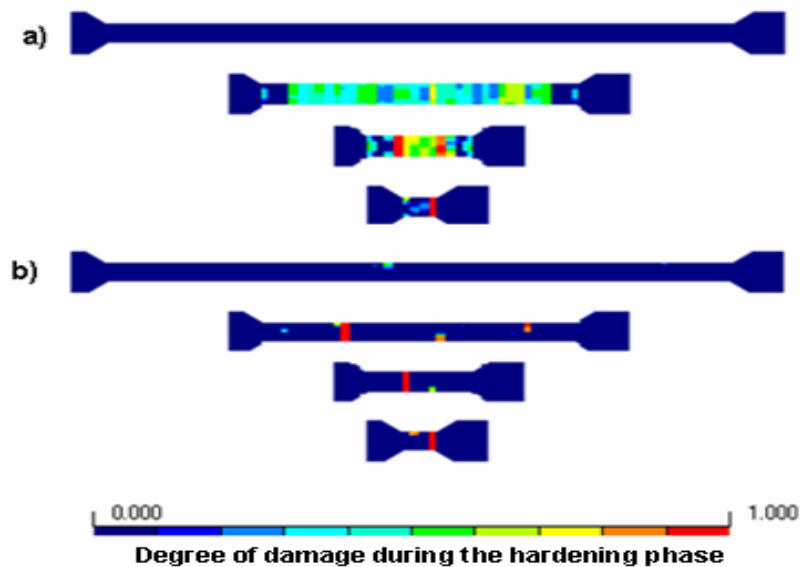


Figure 25: Comparison of the evolution of the fracture energy ( $G_f$ ) with the length of the specimen for both “homogeneous material model” and “statistically distributed tensile strengths model”.



**Figure 26: Comparison between damage induced during the hardening phase at an imposed displacement of 4 mm: (a) constant material parameters, (b) statistically distributed tensile strengths.**

As conclusion, effective (macroscopic) material parameters (tensile strengths, magnitude of hardening, fracture energy) are significantly lower in the case of statistically distributed strengths than in the homogenous model.

The effective strengths are lower because in the “statistical model” many regions (FE) have smaller tensile strengths than the mean values. These weak elements are the first to be attained by the non-linear effects (hardening and later softening). Since damage starts in these elements, tensile stresses drops slowly in the specimen, and the further behaviour of the entire specimen is mainly governed by the already damaged elements. After a certain state, the sound FE unload progressively while the other processes in the hardening regime and later in the softening phase. In other words, in case of the “statistical model” the mechanical behaviour of the specimen is predominantly governed by the weakest regions. The reduction of the fracture energy ( $G_f$ ) is directly related of the reduction of the tensile strength.

For the same reason, the magnitude of the hardening domain, because of the early degradation of the weakest FE, tensile stresses decrease in the whole specimen, consequently, FE with higher strengths unload linear elastically, they cannot exploit their hardening domain. This is clearly evident for the Figure 26 showing distribution of hardening-induced damage in both models. In case of the “homogeneous model”, the hardening regime overruns almost the entire volume of the specimen, while regions in hardening phase are relatively rare in the specimens of the “statistical model”. This rareness is much more pronounced for longer specimens. These effects explain the reduction of the magnitude of the hardening phase in the case of statistically distributed tensile strengths.

*Further and deeper developments are needed for a better understanding of the influence of the statistically distributed material parameters on the macroscopic response of the mechanical behaviour of the material.*

---

### 3. FLEXURAL BEHAVIOUR OF UHPFRC MONOLITHIC BEAMS

#### 3.1 Introduction

The knowledge of the realistic tensile behaviour of materials is one of the main required input to design or to prevent damage in civil engineering structures. This is the case especially for *UHPFRC* which were developed for their high resistance and deformability under tension. To benefit efficiently from these potentials, efforts must be done to characterise as better as possible the material properties. Experimental determination of the tensile properties is rarely carried out by direct tension specimens under controlled deformation because of many factors such as the use of an appropriate very stiff testing machine and time-consuming. Another indirect way to assess tensile material properties is to use 3 or 4 point bending test beams. In normal cement-based materials and conventional FRC, the bending test of beams had proved to be a reliable way and relatively easy to carry out for determining tensile behaviour. The extraction of the tensile properties from the force-deflection curve of bending test beams is performed by an inverse analysis combined with a finite element code.

Due to the complex non-linear behaviour of the *UHPFRC*, simple analytical approaches to carry out an inverse analysis can only provide a first rough estimate of the tensile properties and the characteristic length involved in more detailed analytical calculations lack a fundamental basis of definition and remain empirical at the present stage. On another hand, the Finite Element method combined with an appropriate back analysis algorithm is a powerful tool to perform this kind of inverse analysis.

This chapter is devoted to the inverse analysis of two different types of flexural tests with four different materials. *The modelling of the flexural members is realized by means of the smeared crack model with bulk energy dissipation and no statistical variation of the properties. The model is applied uniformly on the specimens, without predetermination of the localization for 3 point bending tests, and with predetermined bands with a slightly weakened tensile strength for 4 point bending specimens.*

#### 3.2 Inverse analysis with MLS

##### 3.2.1 Procedure

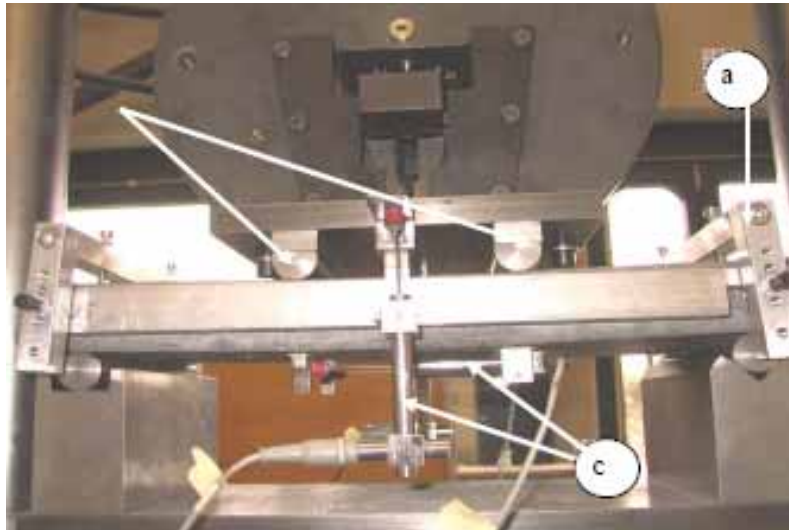
To our knowledge no non-linear commercial F.E. code exists with an implemented algorithm to perform an automatical back analysis, especially for tension hardening-softening materials such as *UHPFRC*. This is also the case of the MLS-FE-Code which will be used along the following computations. As a matter of fact, the number of parameters required to characterize the tensile hardening-softening law of *UHPFRC*, even with a simple quadrilinear model is high and it is probably safer to do the inverse analysis gradually step by step “by hand”.

The procedure consists on idealizing the tested beam by a F.E.-mesh and imposing on it the real mechanical boundary conditions (supports and incremental loading). In these following analyses, the easily measurable mechanical properties such E-modulus, Poisson’s ratio, compressive strength are directly used as input data for the code. The Young’s modulus is adjusted

to fit as well as possible to the linear part of the experimental force-deflection curves. For the first run of the analysis, the parameters of stress-strain hardening-softening law of the material are either taken from uniaxial tensile test (if available) or “consciously” chosen. The resulting numerical load-deflection curve is compared to the experimental one. Then the input material parameters are judiciously stepwise adjusted to approximate the experimental curve. This procedure is repeated several times until a good agreement between measured and simulated curves is found. It must be outlined that this procedure is extremely time-consuming because of the large number of “unknowns” parameters of the stress-strain hardening-softening diagram.

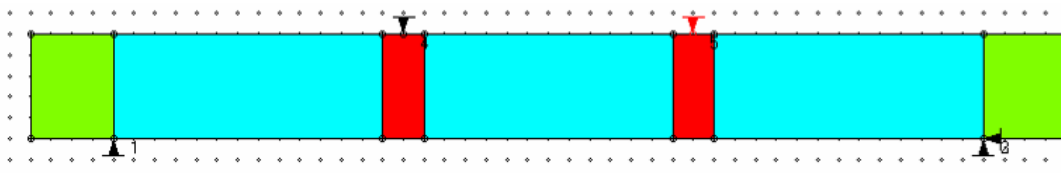
### 3.2.2 Four point bending plates with UHPFRC CEMTEC<sup>multiscale</sup>®

Figure 27 shows the experimental 4 PT bending set-up used at MCS-EPFL, Wuest (2004a) for bending tests on plates.



**Figure 27:** Experimental set-up for 4-point bending tests on plates, Wuest (2004a)

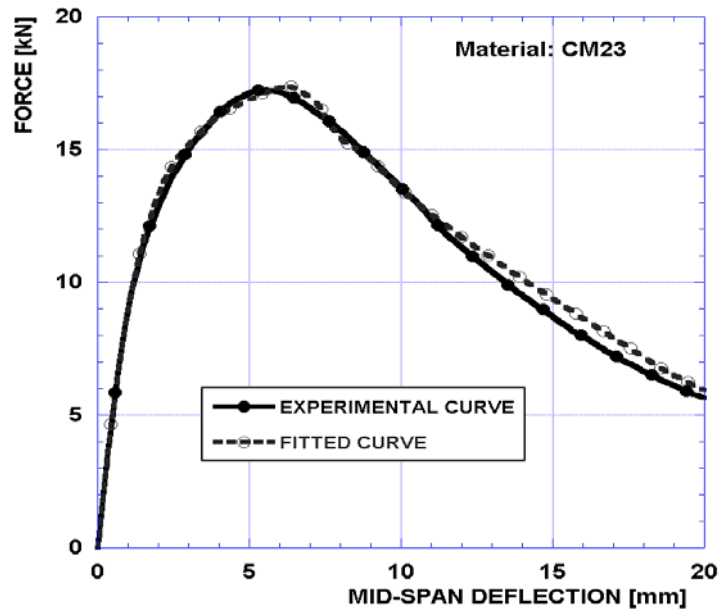
The considered beams have the following dimensions, span-length: 420 mm, width 200 mm and depth of 30 mm. The geometrical and loading configuration of the numerical model is shown in Figure 28.



**Figure 28:** Geometrical and loading configuration of the UHPFRC monolithic beams and its subdivision in macro-elements.



For the case of 4 point bending, to avoid an unrealistic delay of the localisation, *two predetermined bands with a slightly weakened tensile strength are generated under the points of application of the imposed displacements*. With this procedure, the volumetric dissipation is correctly represented and comes to an end according to the variability of the material, otherwise not represented in the model. Figure 29 shows the close correspondance between the fitted and measured Force-deflection curves.



**Figure 29:** Comparison between the experimental (average curve) and fitted Force-deflection curves for the material CM23 cured at 20<sup>0</sup>C at an age of 28 days, Wuest (2004b).

### The constitutive tensile law obtained by inverse analysis is compared on

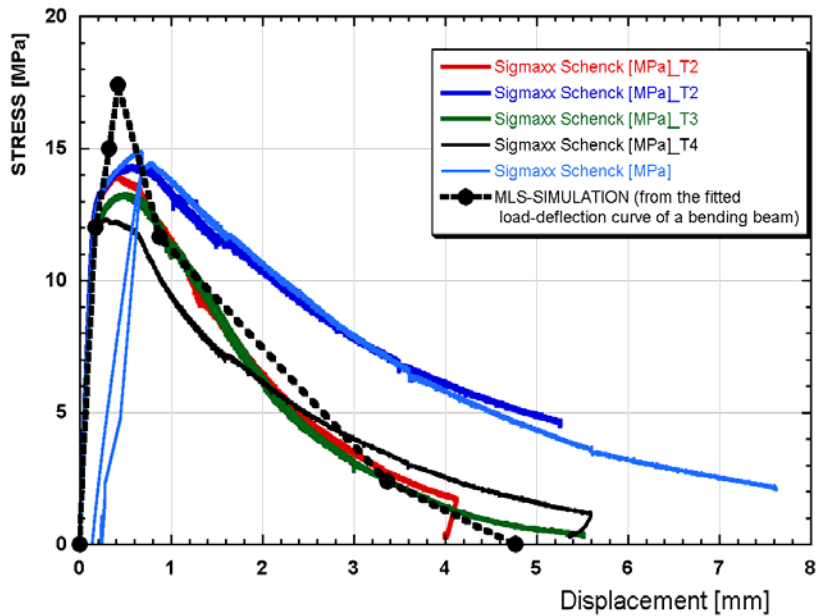
Figure 30 with experimental uniaxial tensile tests results for the same material, SAMARIS D22 (2005). The tensile model determined by inverse analysis corresponds well to the overall tensile response obtained experimentally and follows perfectly the softening response of the three specimens (red, blue and green curves), which had a similar softening behaviour. These specimens exhibited post-peak a localized fracture in one narrow band, which corresponds well to the numerical model.

The two specimens with significantly higher values of the softening response (blue curves) had a more complex fracture behaviour with crack face bridging phenomena, not represented by the numerical model. This can explain why their response significantly differs from the model.

The peak tensile strength of the model is higher than the average measured value, but the extend of the strain hardening domain is very similar to the average measured one.

---

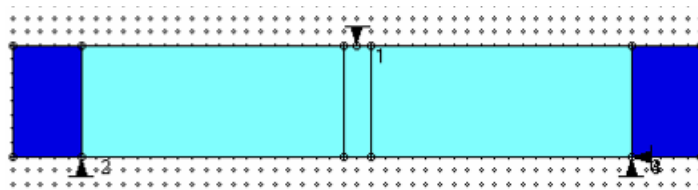
One must emphasize that it is seldom possible to find a perfect correspondance between constitutive tensile laws obtained from inverse analyses and from uniaxial tensile tests. This is especially true for materials with complex fracture behaviour such as UHPFRC.



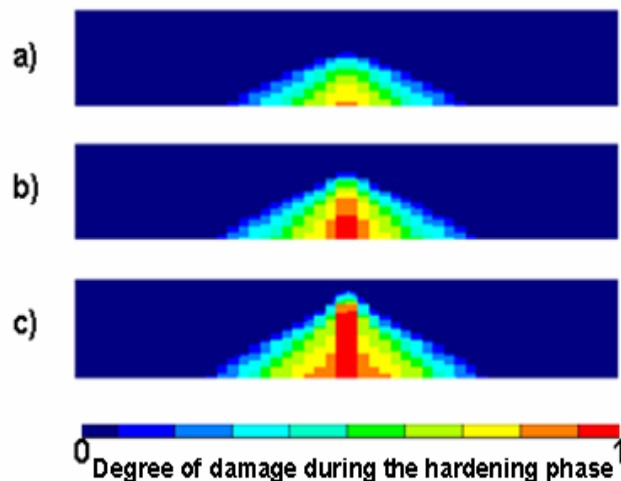
**Figure 30:** Resulting stress-displacement hardening-softening laws for material CM23 cured at 20<sup>0</sup>C at an age of 28 days, deduced from back analyse (Figure 29) and experimental curves obtained from uniaxial tension specimen, SAMARIS D22 (2005).

### 3.2.3 Three point bending beams with UHPFRC DUCTAL®

Two types of the UHPFRC DUCTAL® (A and C) for which experimental Force-deflection curves are available in the literature, Orange et al. (2000) are analysed. Experimental investigations have been performed on 3-points bending beams loaded under controlled displacement, with a total length of 250 mm (span length 200 mm), the width and the thickness are both equal to 40 mm. It must be indicated that in the original figure taken from Orange et al. (2000), the flexural load was given in terms of “equivalent stress” and converted for simulation need into flexural force. The simulation of the test is performed by MLS-Code. Figure 32 shows the evolution of damage induced during the hardening phase at three levels of the imposed displacements, 0.2, 0.3 and 0.6mm. As the imposed displacement increases, damage progresses gradually towards the upper layers of the specimen. During this process, the width of the damaged regions remains quite the same.



**Figure 31: Schematic representation of the 3-point bending beams used to determine mechanical properties of DUCTAL® (A and C)**

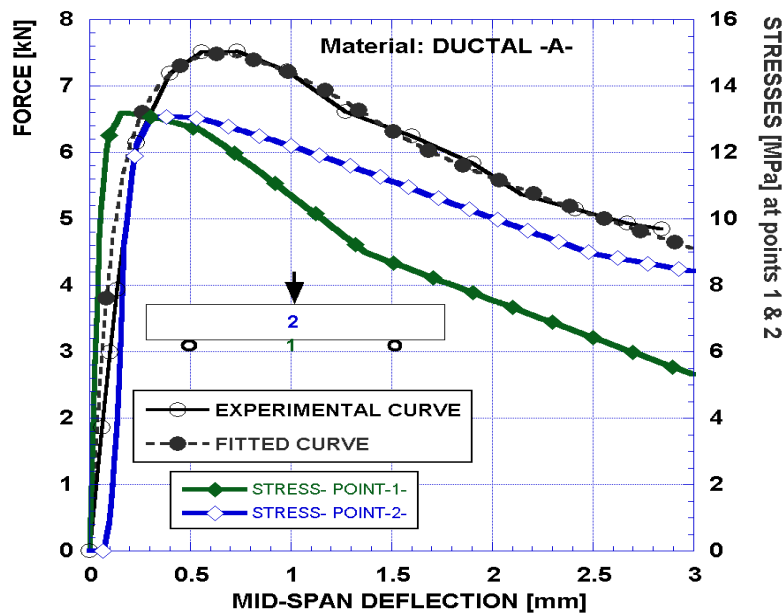


**Figure 32: Distribution of damage in the material DUCTAL®-A at imposed displacement levels of: a) 0.2, b) 0.3mm and c) 0.6.**

Several sets of numerical values of the material parameters have been tried to find out the best the correspondence between the experimental and the simulated load-deflection curves. By using a purely linear hardening law in the modelling, no good correlation between measured and computed force-deflection curves could be found. A bilinear strain-hardening combined with a tri-linear strain-softening diagram gave the best results. The resulting simulated force-

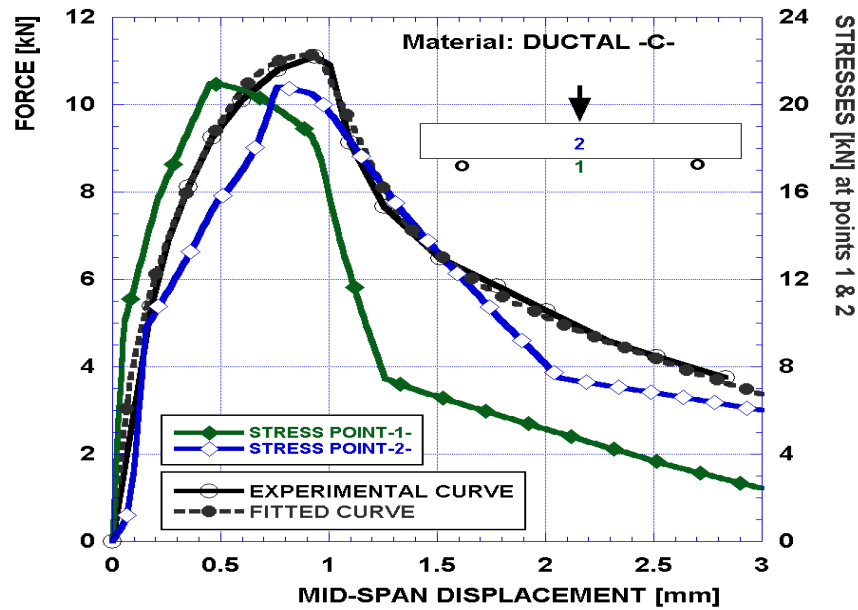
deflection curve is given in Figure 33 and compared with the experimental one. We can notice the good agreement between both curves. The simulation reflects faithfully the pre and post-peak behaviours of the specimen. The maximum flexural load and its corresponding deflection are perfectly predicted by the simulation. In the same figure, the stress evolution at two points (point 1 and 2 in Figure 33) is given.

It must be underlined that points (1) and (2) start to enter in the softening regime much earlier than the maximum flexural load. This fact is extremely important for a realistic prediction of parameters such as “maximum load carrying capacity” or “modulus of rupture” (MOR) and for design of structures in civil engineering field. In other words, the knowledge of elastic and hardening parameters are far to be sufficient even if only the maximum load bearing capacity of a structural member is sought.



**Figure 33: Comparison between experimental and numerical force-deflection curves of DUCTAL®-A bending beam and evolution of stresses at the bottom and in the centre of the specimen (Lvol: 200mm).**

The same back analysis procedure has been used to extract the stress-strain hardening softening law of the material DUCTAL® C. The results are shown in Figure 34 and compared with the experimental curve. As in the former case, a good agreement between simulation and experiments is obtained.



**Figure 34:** Comparison between experimental and numerical force-deflection curves of DUCTAL®-C bending beam and evolution of stresses at the bottom and in the centre of the specimen; (Lvol: 200mm).

The stress-strain hardening-softening laws of DUCTAL® A and C obtained by the best fits are given in the Figure 35 and correspond to the expected result. With the volumetric characteristic length used in the calculations ( $L_{vol}=200$  mm), the strains at peak stresses are respectively 0.1 % for DUCTAL® – A and 0.34 % for DUCTAL®-C. The material DUCTAL®-C with fibres with improved bonding has a dramatically increased performance. One must however outline the fact that DUCTAL® materials are thermally cured at early age to improve their mechanical performance. As such they cannot be directly compared to UHPFRC cured at ambient temperatures.

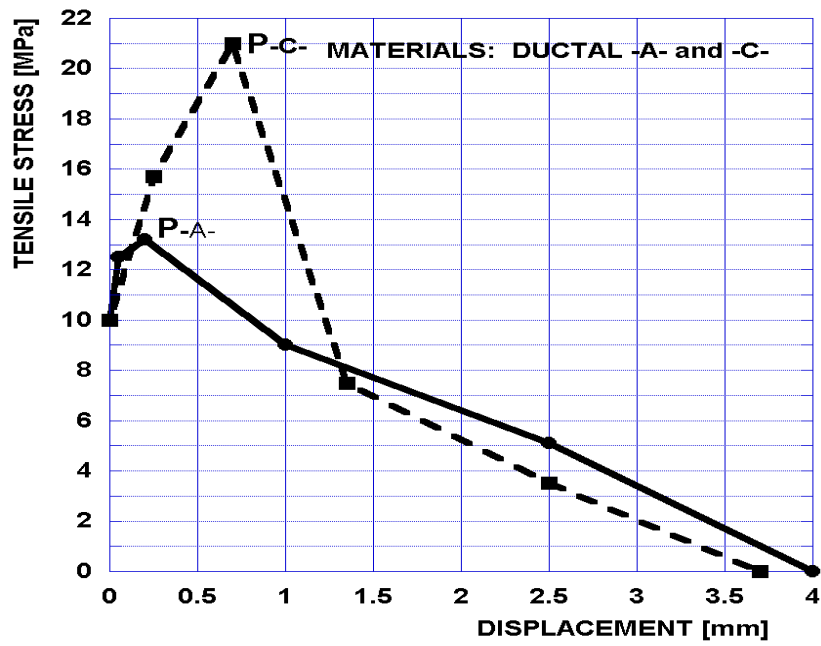


Figure 35: Stress-strain hardening softening diagrams for two UHPFRC obtained from experimental curves by means of an inverse analysis. (volumetric characteristic length  $L_{vol} = 200$  mm).

## 4. TIME-DEPENDENT BEHAVIOUR OF COMPOSITE UHPFRC-CONCRETE BEAMS

### 4.1 General

The main objective of this chapter is to assess the early mechanical behaviour of composite beams consisting on cast fresh UHPFRC layer on the surface of an old conventional reinforced concrete beam.

### 4.2 Overview of existing works

The numerical modelling of the structural behaviour of bonded concrete overlays and more generally of composite concrete-concrete structural members has been realized in various ways in the past, with either general purpose finite element packages, specifically oriented packages for multi-layer systems, or original numerical solutions of mathematical formulations of the problem. Basically, any finite element package is able to model multi layer systems. The main differences come from the ability of the software to deal with more advanced material properties such as:

- Time-dependent evolution of the mechanical properties of the overlay and substrate - maturation
- Comprehensive simulation of the physical processes such as drying, release of heat of hydration, thermal transport,
- Viscoelasticity and ageing
- Non-linear crack propagation (smeared crack models or discrete crack models)
- Interface between two layers
- Reinforcement bars

It is impossible to quote all modelling works on composite systems however, among the most recent ones, one can mention the following:

Martinola (2000), Martinola et al. (2001) used FEM package DIANA (1996) for thermo-hygro-Mechanical calculations with a strong emphasis on moisture transport and self-desiccation, in order to study the risk of cracking and delamination of composite structural systems with concretes of different ages. Realistic interfacial constitutive laws were used with parameters from experimental tests. Based on comprehensive experimental tests, the hygro-mechanical coupling coefficient was implemented in the code as a function of the moisture content, and the major influence of its variation was demonstrated. A parametric study was performed and recommendations for the design of bonded concrete overlays were given.

Laurence (2001) used software CESAR –LCPC to calculate the evolution of stresses at early age and long term in bonded concrete overlays. The modules TEXO, MEXO and HEXO of the finite element package were used to calculate the stresses induced by thermo-chemo-mechanical effects at early age, taking maturation into consideration, for linear elastic materials. In a second step, the effect of drying shrinkage, including water absorption by the substrate, was introduced. The results showed the very significant influence of autogenous

---

shrinkage as well as of the absorption of water by the substrate on the development of stresses in the overlay.

HIPERPAV, Rasmussen et al. (1995) although not a finite element code, takes into consideration thermo-hygro-mechanical phenomena by means of semi-empirical mathematical formulas from codes or recommendations, to predict the risk of cracking in overlays. The physical processes involved (thermal and moisture transport) are based on semi-empirical analytical solutions for current geometries.

The model from Rostasy et al. (2002) is also numerical-analytical but includes very comprehensive descriptions of the physical and mechanical phenomena acting at early age and long term in composite structures. Although more dedicated to massive structures, walls on slabs for instance, this model is also applicable to overlays on substrates.

### 4.3 Modelling of time dependent behaviour with software MLS

Software MLS has been specially developed for multiple layer systems with cementitious materials of different ages.

Numerical modelling in software MLS, Figure 36, is based on two main aspects:

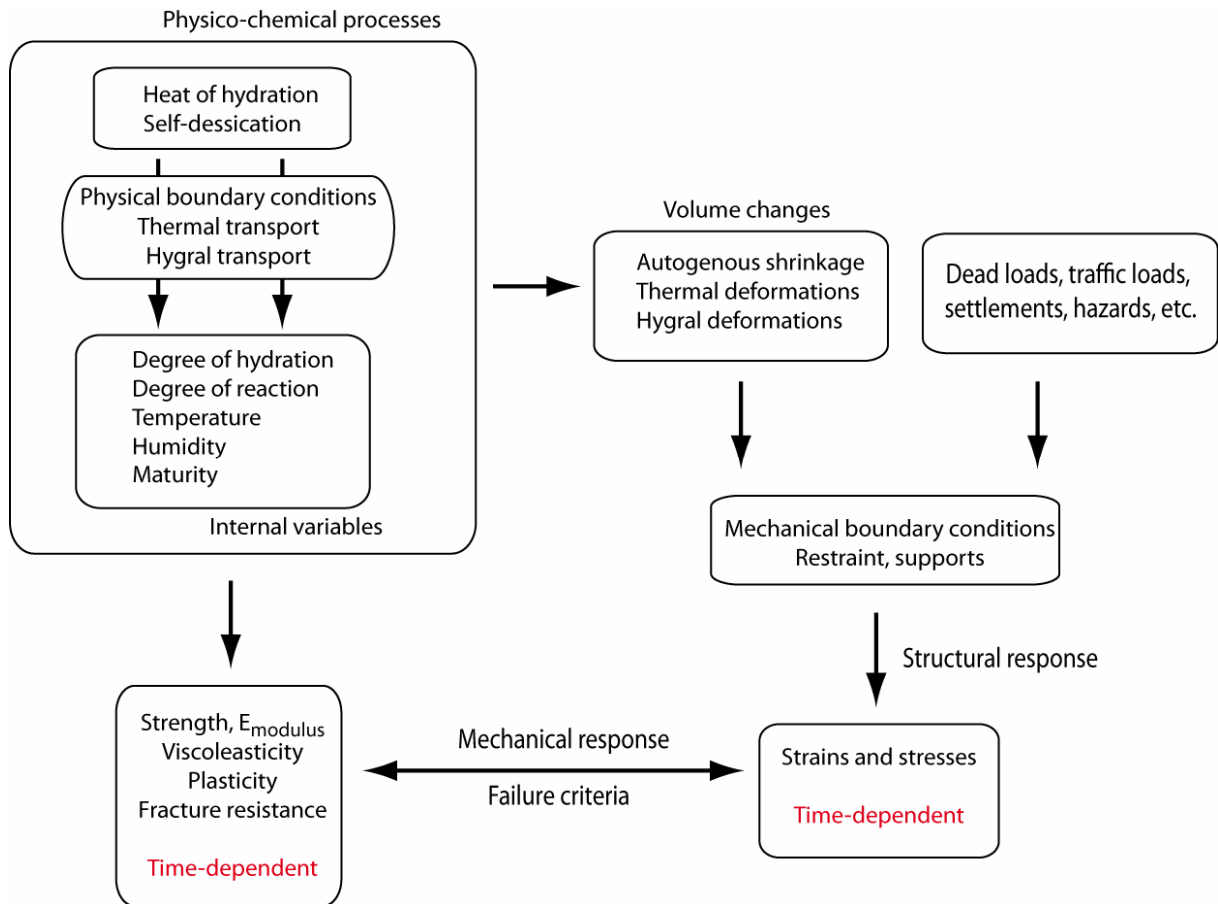
- physico-chemical phenomena
- mechanical response

*The physico chemical phenomena* involve thermal and hygral transport, as well as the dissipation of the heat of hydration and self-dessication. The associated “internal variables” of the program are the temperature, the humidity, the degree of hydration and the maturity defined on the basis of an Arrhenius model. These phenomena influence both the maturation of the material with a dependency of the mechanical properties on the maturity, and the volume changes calculated by hygro or thermo mechanical coupling coefficients or directly through the input of maturity dependent autogenous shrinkage.

*The mechanical response* is given by the interaction of the structural response of the model (effect of external load and restrained volume changes) which determines the local evolution of strains and stresses, and the time dependent evolution of the strength, elastic modulus, viscoelasticity and fracture resistance.

Multiple couplings can be defined between the various parameters and models in the program. Their detailed description can be found in Bernard (2000).





**Figure 36: Actions, effects, and main parameters in a composite structural member with cementitious materials of different ages.**

Bernard (2000) used software MLS, for the simulation of composite members with concrete layers of different ages, with a comprehensive description of thermo-hygro-mechanical processes in multi-layer systems, at early age and long term, including effects of maturation, viscoelasticity, reinforcement in the overlay and non-linear fracture mechanics (smeared crack model) for the bulk of the materials and for interfaces. The very significant role of autogenous shrinkage of concrete at early age on the structural response of composite elements and the consequences of the restraining effect of reinforcement bars in the new layer were demonstrated. The results include an extensive parametric study on the effect of the overlay thickness and reinforcement ratio on the risk of delamination.

Habel (2004) used the same finite element code to model the time dependent response of composite UHPFRC – Concrete beams with various geometries and degrees of restraint, for one type of UHPFRC (CM0), and for the inverse analysis of restrained shrinkage tests to determine the ageing viscoelastic response of UHPFRC at early age, Habel et al. (2006a, 2006b). *The calculations for composite structural members showed that significant eigenstresses develop in UHPFRC overlays, and that reinforcement bars increase this effect. These eigenstresses slowly vanish after several years.*

---

In a further step, it was decided to study more in depth the effect of eigenstresses in composite UHPFRC-concrete members, with the new version of the MLS software including tensile stress-strain hardening softening model, with two main objectives:

- 1) Determine the effect of eigenstresses on the mechanical response of composite UHPFRC-concrete members under flexural loading, and make inverse analyses of fracture tests, with eigenstresses.
- 2) Determine the influence of an overdepth of the substrate on the development of eigenstresses in composite UHPFRC concrete members

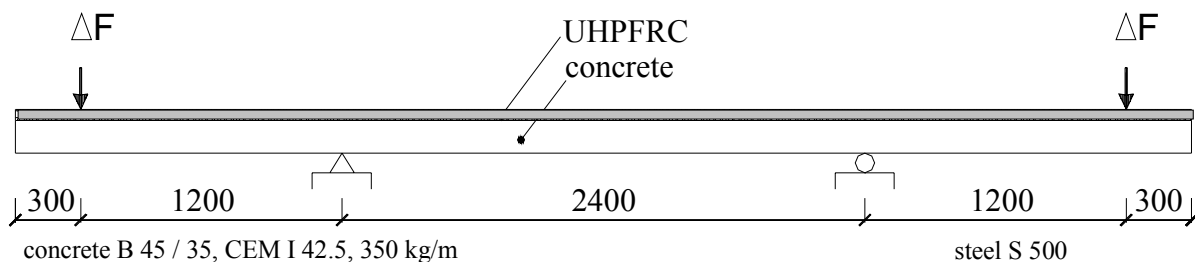
*The second task could be achieved, but the first task could not be terminated due to technical problems with the couplings of the fracture and viscoelastic models. These problems have been solved meanwhile and research is now ongoing on task 1. As a consequence, in this report, for task 1, only the calculations associated to eigenstresses are presented.*

## 4.4 Analysis of composite beams

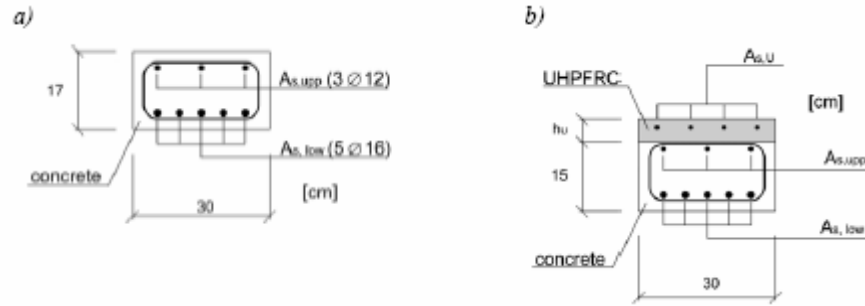
### 4.4.1 Beam geometry

Composite beams with a length of 5400 mm, consist on an old conventional reinforced concrete beam with a thickness of 150 mm with an UHPFRC overlay. The thickness of the overlay is varied with 30 and 50 mm

The composite beam is supported vertically and monitored by electronic devices recording continuously deformations such as deflection, upthrust, warping, shows schematically the geometry of a typical composite system. Procedures concerning the preparation of the composite beams and the measuring set-up are described in detail in SAMARIS Reports D18a (2004) and b(2006). UHPFRC-overlays with a thickness of 50 mm are reinforced with steel bars. The distribution of steel bars in the substrate and in the thicker overlays is shown in Figure 38.



**Figure 37: Schematic representation of the composite UHPFRC-concrete beams used in experimental investigations**



**Figure 38: Positions and dimensions of the steel reinforcement bars in a cross section (a) in the substrate, (b) in the composite beam, SAMARIS D18b (2006).**

#### 4.4.2 Initial and boundary conditions

Experiments have been performed at room temperature varying from 20 to 22°C. Before casting of the overlay, the substrate is in thermal equilibrium with its surroundings (around 21°C). Due to the mechanical energy induced by the mixing operation of the UHPFRCC components, the measured temperature of the UHPFRCC paste at casting is roughly 5°C higher than the initial temperature of the components (room temperature). The whole system is exposed to room temperature.

- Hygral and thermal transport are considered for the concrete substrate.

- For the UHPFRC, only thermal transport is considered for two reasons. Firstly, scarce data is available on moisture transport properties of UHPFRC (diffusion coefficient, desorption isotherm). Secondly the moisture transport in UHPFRC is minor at early age with minor hygral shrinkage after 7 days (usual period of moist curing for these materials), and negligible hygral shrinkage after 7 days.

The following thermal and hygral initial and boundary conditions are considered in the simulations:

*Temperatures:*

$$T_{\text{UHPFRC}}(t=0) = 26^{\circ}\text{C}$$

$$T_{\text{SUBSTRATE}}(t=0) = 21^{\circ}\text{C}$$

$$T_{\text{EXTERNAL}}(t) = 21^{\circ}\text{C}$$

*Heat transfer coefficient ( $\pi_{T,\text{transfer}}$ ) applied to the surfaces of the beam in contact with surrounding the atmosphere:*

$$\pi_{T,\text{transfer}}(t < 7\text{d}) = 4 \text{ W}/^{\circ}\text{C}/\text{mm}^2$$

$$\pi_{T,\text{transfer}}(t < 7\text{d}) = 8 \text{ W}/^{\circ}\text{C}/\text{mm}^2$$

During the first 7 days, the overlay is covered with a plastic sheet, which reduces slightly heat transfer to the surroundings.

*Relative Humidity:*

$$H_{\text{SUBSTRATE}}(t=0) = 95\%$$

$$H_{\text{EXTERNAL}}(t) = 35\%$$

Humidity convection coefficient ( $\beta_{H,\text{transfer}}$ ) applied to the surfaces of the beam in contact with the surrounding climate:

$$\pi_{H,\text{transfer}}(t < 7\text{d}) = 0 \text{ (sealed)}$$

$$\pi_{H,\text{transfer}}(t < 7\text{d}) = 10^{-8} \text{ 1/mm}^2 \text{ (value generally used for normal concrete in calm atmosphere)}$$

*Mechanical boundary conditions:*

Different mechanical boundary conditions have been used during the simulation. They will be mentioned in each considered case.

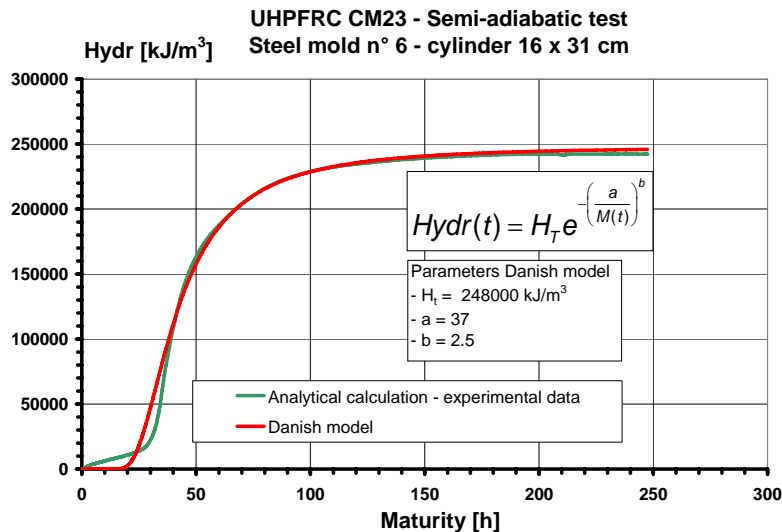
#### 4.4.3 Material parameters

##### (a) Concrete-Substrate

The substrate is a reinforced concrete beam, with an old concrete. No ageing effect has been considered since the material was minimum 3 month old at the casting of the UHPFRCC layers during the tests.

##### (b) UHPFRCC-Overlay

Material CM22 has been used for the overlay. Its physical and mechanical properties have been directly measured or deduced from experimental results by means of inverse analysis. The heat of hydration model determined on UHPFRCC CM23, with a closely similar composition, SAMARIS D22 (2005), was used. Figure 39 shows the evolution of the heat of hydration as a function of maturity for UHPFRCC CM23.



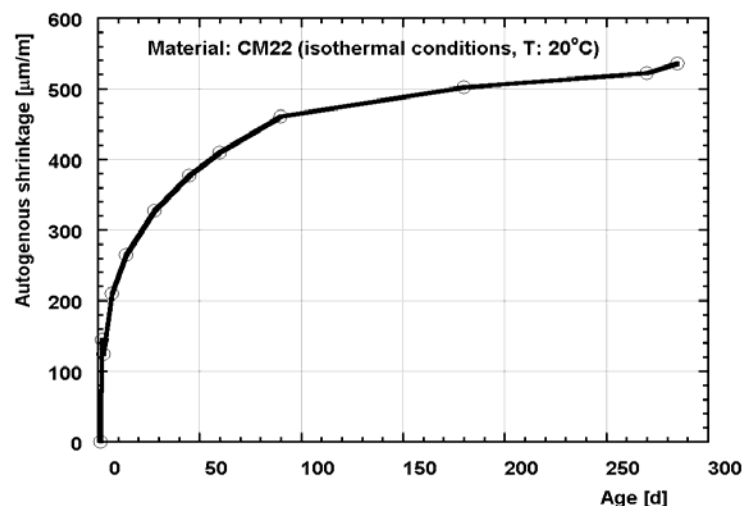
**Figure 39:** Measured heat of hydration under semi-adiabatic condition and comparison with Danish model obtained by means of numerical analysis, SAMARIS D22 (2005).

The stress-strain hardening-softening law at 28 days were fitted from experimental results according to the procedure demonstrated in chapter 4. Its dependency on the age (maturity) is assumed to follow the same evolution as the tensile strength ( $\sigma_{cc}$ ), according to MLS-code. This former material parameter has been measured as function of the age, as well as the other mechanical parameters introduced in the simulations: Young's modulus, compressive strength and viscoelastic properties, Habel et al. (2006a, 2006b), Habel 2004, Kamen et al. (2005).

The unrestrained autogenous shrinkage measured under isothermal conditions (20°C) shown on Figure 40, Kamen et al. (2005), is used in the thermo-mechanical simulations.

The influence of temperature on the autogenous shrinkage is considered by means of a dependency on the maturity (defined by an Arrhenius function with an activation energy  $Q/R=4000$  K). *The influence of temperature on autogenous shrinkage is not yet fully understood and the applicability of maturity models is questioned by several authors.*

*However, no better models are currently available and this dependency is not of major importance for thin UHPFRC layers (3 to 5 cm) for which the maximum temperature elevation at early age does not exceed 5 °C. This would of course not be the case for thicker UHPFRC elements for which further investigations would be needed.*



**Figure 40:** Measured free autogenous shrinkage for UHPFRC CM22. Note: the setting delay of 30 hours for the start of the autogenous shrinkage has been considered but cannot be seen on the figure.

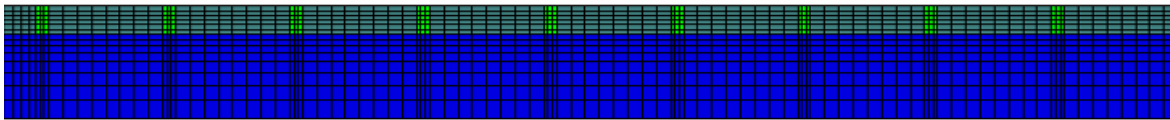
#### c) Interface between the substrate and the overlay

The tensile strength of UHPFRC-concrete interfacial zone has been determined experimentally by Habel (2004) on composite specimens of various types (direct tension and wedge splitting tests). In all cases, no bond failure occurred and the value of the maximum tensile strength of the substrate where failure took place was found to be greater than 2 MPa, which is much higher than in the case of a mortar-concrete interface (less than 1 MPa).

---

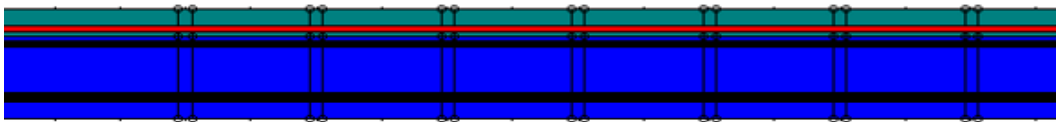
#### 4.4.4 Finite element mesh

Figure 41 shows a partial view of the FE mesh of the slender composite beams. Different FE-sizes have been used in order to minimize the total number of elements and consequently to reduce the computational time. The numerical analysis of these slender elements is relatively time-consuming due to the nonlinearity and the coupling of the equations governing the thermo-mechanical processes.



**Figure 41:** Visualisation of the mesh of a part of the slender composite beam. It is composed on 2842 F.E. with different sizes (overlay in green, substrate in blue) and on 203 interfacial elements along the interface between the overlay and the substrate.

In MLS-code the reinforcement bars can easily be introduced in a structural member, just by defining the effective thickness of the bars and their position. Figure 42 shows the embedded steel bars, red coloured in the UHPFRC and black in the substrate. In MLS, mechanical properties of the reinforcing bars and bond-slip laws are considered.



**Figure 42:** Position of steel reinforcement bars (black in the substrate and red in the UHPFRC-overlay).

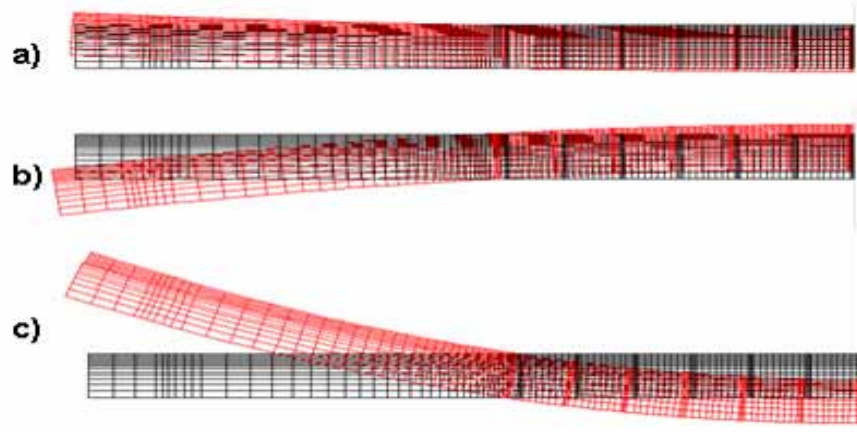
#### 4.4.5 Effect of the structural boundary conditions and reinforcement bars

Thickness of the UHPFRC-overlay: 50 mm, Steel bars reinforcement in the UHPFRC-overlay; composite system with two supports.

In this analysis, the UHPFRC overlay is reinforced by steel bars and the composite beam is restrained vertically at 2 points localized symmetrically on the down surface of the substrate (Figure 37).

Figure 43 shows deformed shapes of the left part of the composite system at three different ages, 12, 28 and 72 hours. The short (age) evolution of the end-span and mid-span displacement are given in Figure 44, points (a), (b) and (c) in this figure are related to the shapes shown in Figure 43. At 12 h, the whole system is in cooling phase due to the initial temperature difference between the fresh UHPFRC (26°C) and the overlay (21°C). At 28h, the system is in a swelling state due to the rise of temperature liberated during hydration. After roughly 45 hours, the main part of the heat of hydration is liberated, the whole system is al-

most in thermal equilibrium with surroundings and the autogenous shrinkage becomes the predominant driving force governing the mechanical behaviour of the system. The induced deformations provoke a curvature of the entire system, as shown in Figure 43c, leading to an upthrust of the end-spans and a deflection in the mid-span region. The middle term evolution of the deformations is plotted in Figure 45. The partially substrate-restrained deformation of the UHPFRCC –overlay induces in the new material relatively high eigenstresses. Figure 46 shows the stress distribution in the system at 30 and 180 days. The substrate is in a compression state, while the overlay is subjected to tensile stresses. The interfacial region of the overlay material undergoes the highest tensile stresses than the upper regions. The evolution of the highest tensile stress in the overlay as function of age is plotted in Figure 47. The induced stresses are important (more than 4 MPa), but due to the high mechanical performance of the UHPFRCC, stresses lie under the tensile strength of the material (see dashed curve representing the evolution of the tensile strength ( $\sigma_{cc}$ ) of CM22 in Figure 47), meaning that neither hardening-induced damage nor crack formation can occur for this geometrical and structural configuration. In a comparative simulation, the overlay material has been considered as a linear elastic material (the other properties remain unchanged), the resulting induced highest tensile stress is also plotted in Figure 47. By comparing both results we can clearly notice the highly favourable viscoelastic character of the CM22 material. The viscoelasticity reduces strongly the induced stress, they are at least 50% lower than in the linear elastic case. It must be underlined that due to the tensile strength ( $\sigma_{cc}$ ) of the repair material, the beneficial potential of the hardening response remains available under these “light” conditions of solicitation (no external mechanical or thermal loading).



**Figure 43:** Partial view of the deformed shapes of the composite beam at 12, 28 and 72 hours after the casting operation.

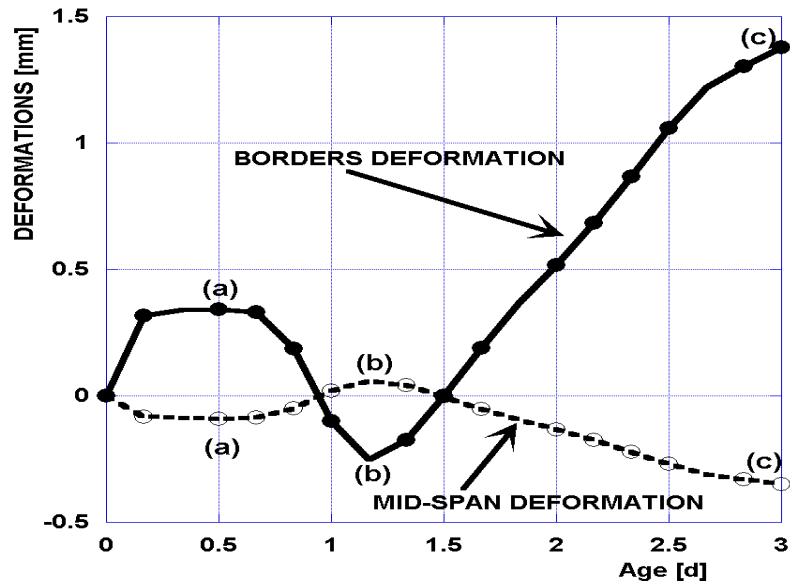


Figure 44: Evolution at short term (3 days) of the mid and end-span deformations of the composite beam induced by thermal effects (liberation of heat of hydration in UHPFRCC and surrounding temperature) and self-desiccation of the overlay.

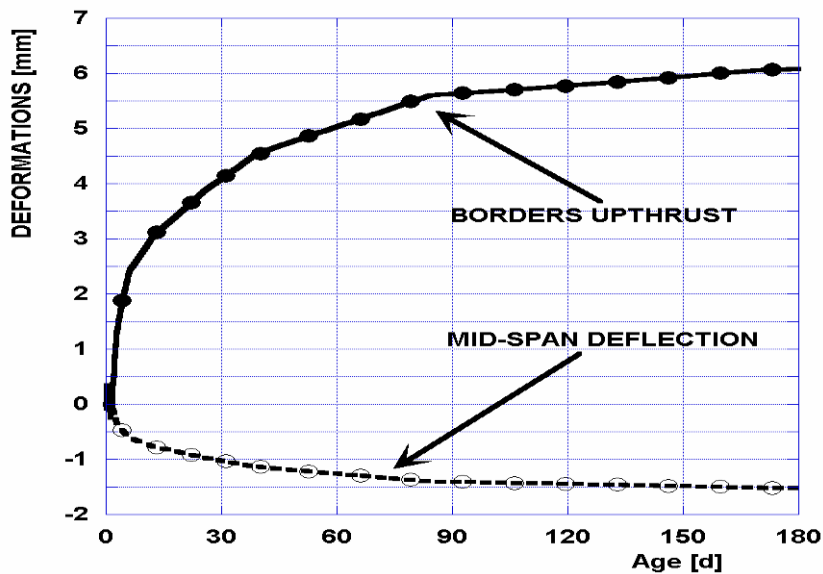


Figure 45: Evolution at a middle term (6 months) of the mid and end-span deformations of the composite beam induced mostly by the autogenous shrinkage of the UHPFRCC.



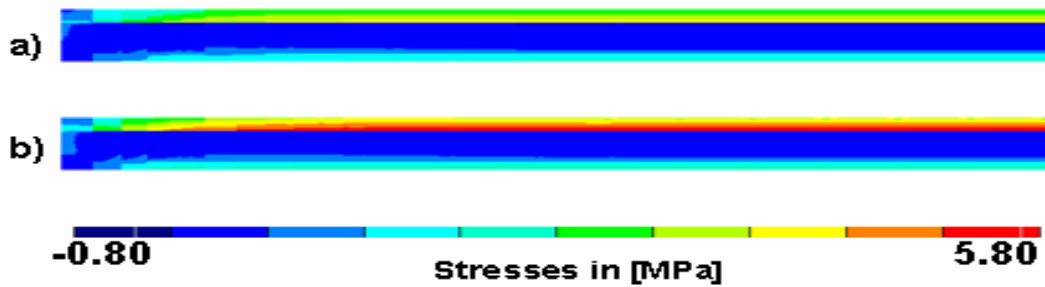


Figure 46: Stress distribution in the left part of the slender composite beam at two ages (a) 30 d and (b) 180 d. UHPFRCC overlay with a thickness of 50mm and reinforced by steel bars. The lower face of the system is supported vertically by two point-supports only.

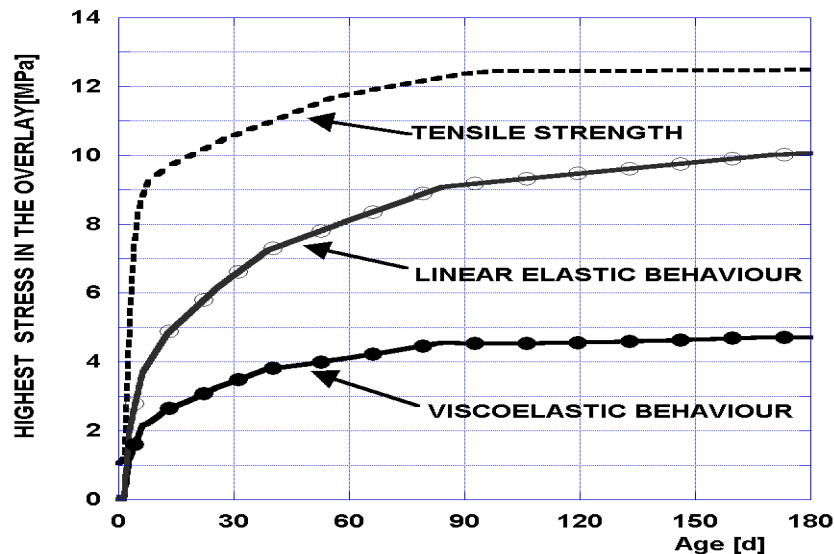


Figure 47: Evolution of the highest autogenous shrinkage-induced eigenstress in the UHPFRCC-overlay and of the tensile strength ( $\sigma_{cc}$ ) of the material as function of age. The curve obtained by considering UHPFRCC as linear elastic material is also plotted in order to underline the beneficial effect of the viscoelastic character of UHPFRCC.

#### Restrained lower face of the system

In the following simulation the degree of restraint of the composite beam is increased by hindering deformations of the lower face of the substrate. Eigenstress distribution at an age of 6 months is given in Figure 48b and compared to the first analysed case, Figure 48a. First, we can notice that the stresses induced by the autogenous shrinkage are much higher than in the simply supported system. Secondly, the whole overlay, apart the end-span zones, is homogeneously stressed, while in the first case a stress gradient is established in the cross section of the overlay (Figure 48a). The evolution of the highest eigenstress as function of age is plotted

in Figure 49 and compared with the first studied case. The increased degree of restraint leads to an increase of the induced eigenstresses by approximately 30%. Also, in this case no damage occurred in the system, due to the high resistance of material CM22.

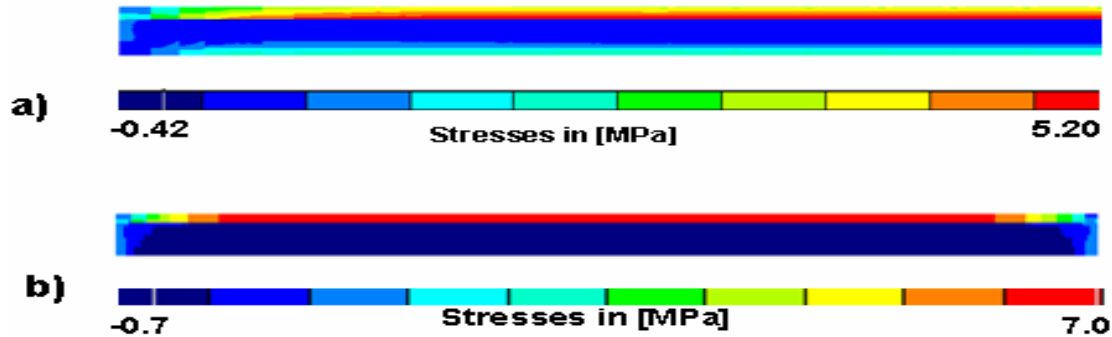


Figure 48: Stress distribution in the left part of the composite beam at an age of 6 months. UHPFRCC overlay with a thickness of 50mm and reinforced by steel bars: (a) lower face of the system is simply supported vertically at two rolling pins, (b) lower face of the substrate totally restrained.

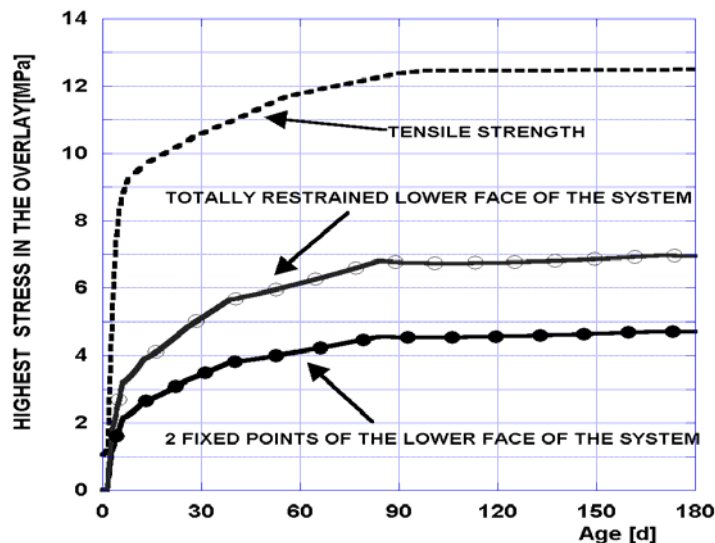


Figure 49: Comparison of the evolution of the highest autogenous shrinkage-induced eigenstress in the UHPFRC-overlay as function of age between two cases of restraint of the lower face of the substrate: totally restrained, restrained vertically at 2 points (by means of rolling pins).

#### Without steel reinforcement bars in the overlay

To study the influence of the steel reinforcement bars, the same composite system has been analysed without bars. Autogenous-shrinkage eigenstress distribution is given in Figure 50 at an age of 6 months and compared with the steel bars reinforced overlay case (Figure 50b).

The eigentress evolution as function of age is plotted in Figure 51 and compared with the free steel bar reinforcement case. We can conclude from the two former figures that the introduction of steel bars leads to higher eigenstresses. This effect is due to the very stiff inert bars which constitute an additional degree of restraint to the shrinking surrounding overlay. Nevertheless, the induced eigenstresses remain lower than the tensile strength ( $\sigma_{cc}$ ) of the UHPFRCC. Steel bars will play a favourable role only in case of cracking.

Figure 52 give the evolution of end and mid-span deformation as function of the age for in both cases. The reinforcement bars in the overlay leads to smaller deformations, due to the increased degree of restraint induced by steel.

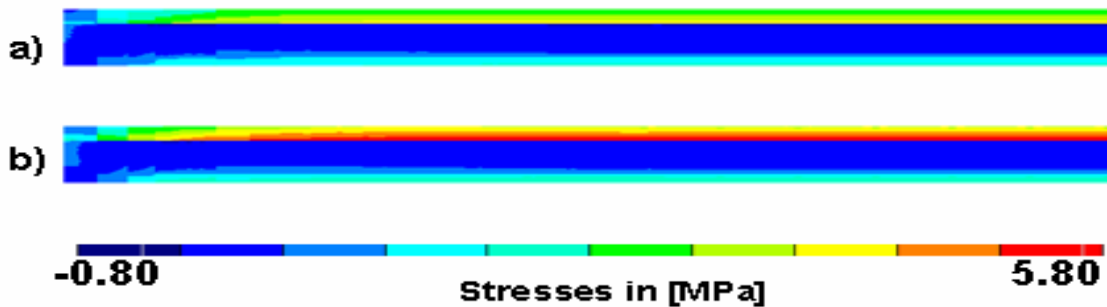


Figure 50: Stress distribution in the left part of the composite beam at an age of 6 months. UHPFRC overlay with a thickness of 50mm (a) without steel bar reinforcement, (b) with steel bar reinforcement.

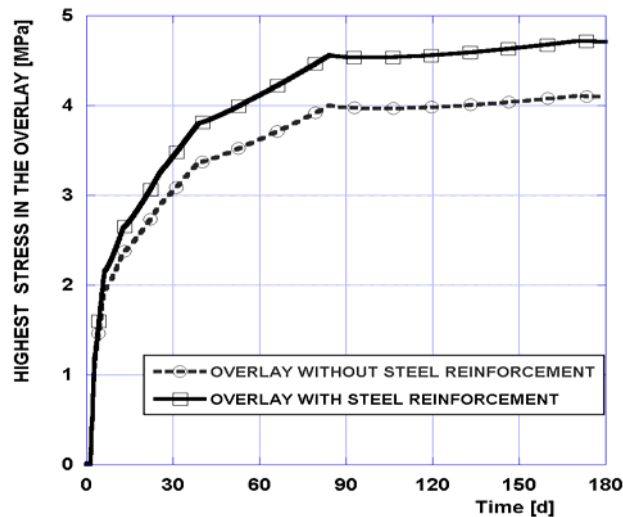
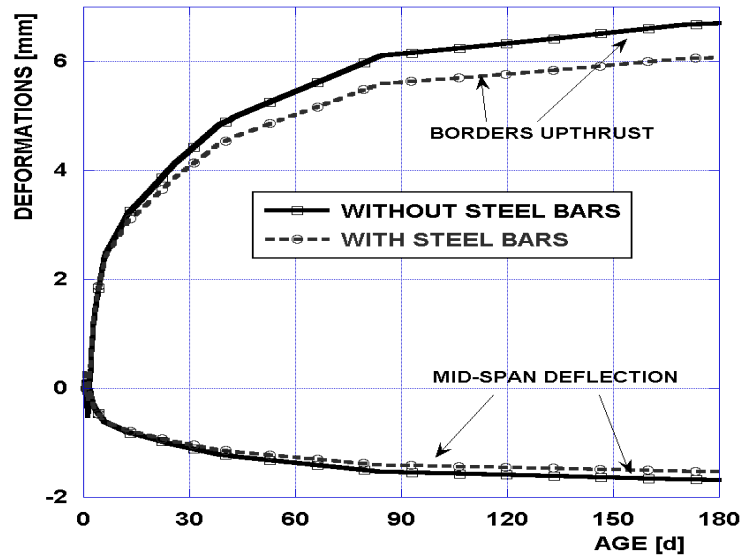


Figure 51: Comparison of the evolution of the highest autogenous shrinkage-induced eigenstress in the UHPFRC-overlay (thickness 50mm) as function of age between two cases: with and without steel bars reinforcement of the overlay.



**Figure 52:** Evolution at a middle term (6 months) of the mid and end-span deformations of the composite beam induced by the autogenous shrinkage of the UHPFRC-overlay with a thickness of 50mm, with and without steel bars reinforcement.

#### 4.4.6 Effect of the thickness of the UHPFRC- overlay: 30 mm

In these simulations, the thickness of the overlay is reduced to 30mm, without steel reinforcement bars. Two different degrees of restraint are considered.

Figure 53 shows the evolution of the end-face and mid-span deformations of the composite beam with two thicknesses of the UHPFRC-overlay, 30 and 50mm. Results show that deformations are larger for thicker overlay. The difference is more pronounced for the end-span deformation. The evolution of the maximum eigenstress is shown in Figure 54 for both degrees of restraint and for overlay with two different thicknesses (30 and 50mm). Stresses in UHPFRC-overlay are higher for thinner overlay, because as it has been demonstrated analytical the degree of restraint is inversely proportional to ratio  $h_{\text{over}}/h_{\text{subst}}$  (ref).

In general these described numerical results are confirmed numerically in the PhD-thesis of K. Habel in the computation have been carried out by the MLS old-version.

.....

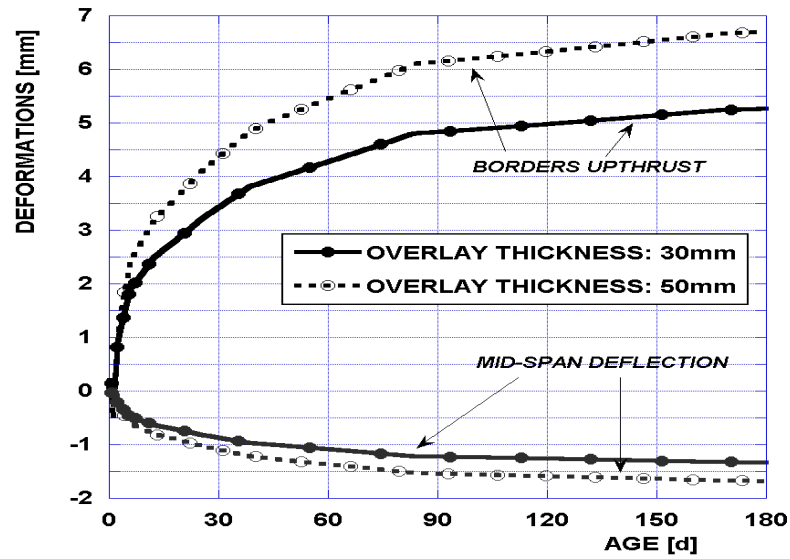


Figure 53: Evolution at a middle term (6 months) of the mid and end-span deformations of the composite beam induced by the autogenous shrinkage of the UHPFRC-overlay with two different thicknesses: 20 and 50mm.

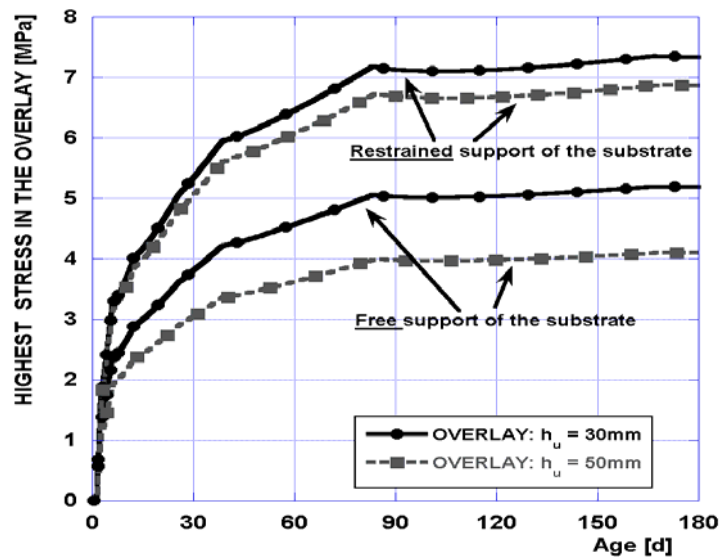
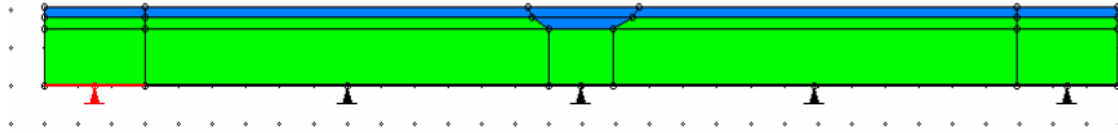


Figure 54: Comparison of the evolution of the highest tensile stress in the UHPFRC with two different thicknesses (30 and 50mm) for two degrees of restraint.

---

#### 4.4.7 Composite beams with an over-depth of the overlay

The geometrical configuration of the composite beam is shown in Figure 55.



**Figure 55: Schematic representation of a composite UHPFRC-concrete beam with an over-depth.**

##### *GEOMETRY OF THE BEAM:*

Length: 3280 mm

Thickness of the substrate: 180 mm

Thickness of the overlay: 30 mm

##### *GEOMETRY OF THE OVERDEPTH:*

Highest length: 330mm (upper surface)

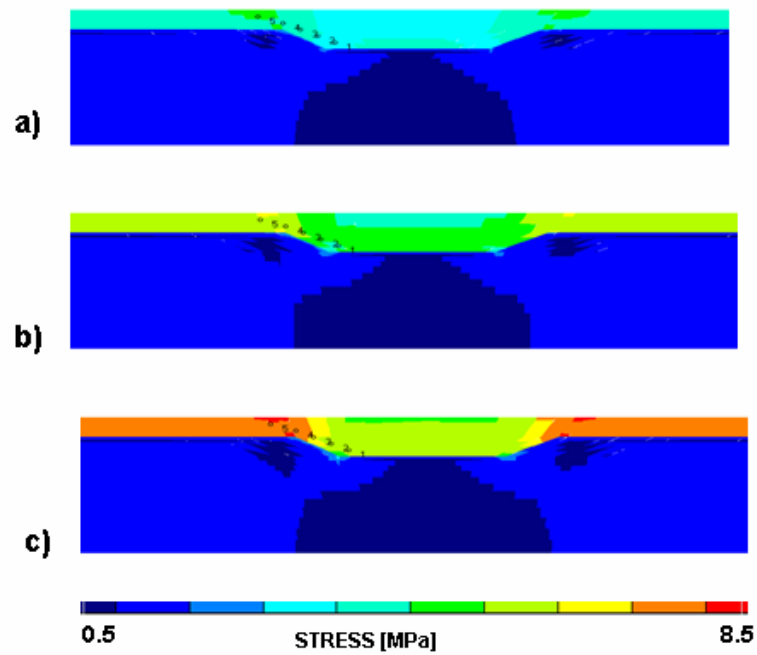
Lowest length: 190 mm (surface in contact with the overlay)

Depth of the CM22 embedded in the substrate: 30 mm

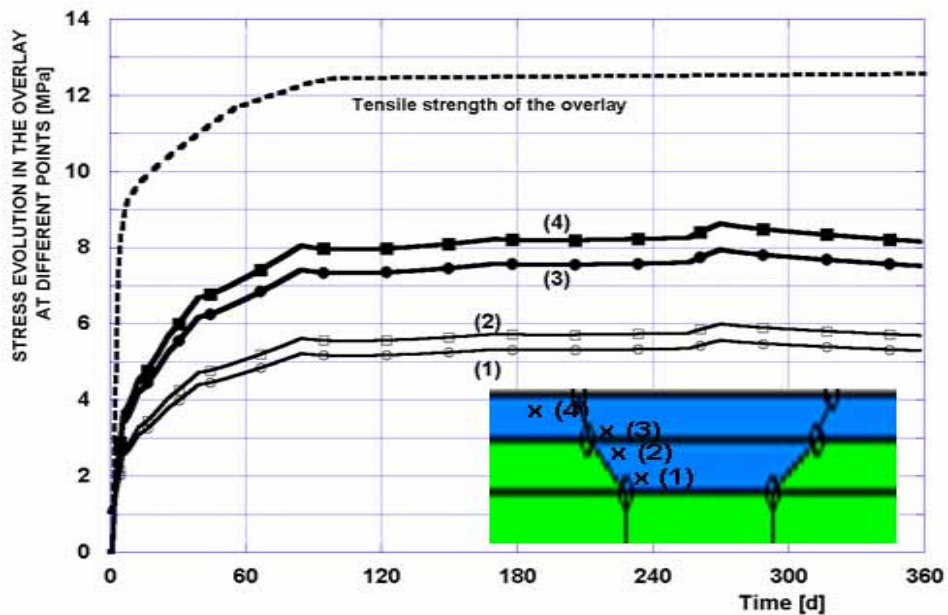
The initial and boundary conditions are identical to those of the composite beams studied above. The lower face of the substrate is totally restrained.

Figure 56 shows the distribution of the autogenous-shrinkage induced eigenstresses at 3 different age, 3, 30 and 100 days (when autogenous shrinkage virtually comes to an end).

The evolution of the eigenstresses in the UHPFRC overlay at different points is shown in Figure 57. In this geometrical configuration, the highest tensile stress is found in the upper surface of the overlay, above the over-depth. This stress is roughly 15% higher than in case of the composite beam without an over-depth. A significant eigenstress-gradient is established along the over-depth cross section (see Figure 57), while in case without a over-depth, the eigenstresses are roughly homogenous along the cross section of the overlay (with thickness of 30mm).



**Figure 56:** Autogenous shrinkage-induced stress distribution in a composite UHPFRC-concrete beam presenting an over-depth, a three different ages (3, 30 and 100days).



**Figure 57:** Stress evolution in the composite UHPFRC-concrete beam with an over-depth at different points.

---



## 5. CONCLUSIONS

- The tensile behaviour of UHPFRC with volumetric and surfacic energy dissipation can be represented in finite element codes by a smeared crack model with adapted characteristic lengths. One length, representative of the volumetric dissipation is constant. The length related to the surfacic energy dissipation is a function of the mesh size such as to conserve the surfacic energy dissipated during the fracture of the material, according to the generalized crack band model of Bazant et Oh (1983).
- The tensile response of UHPFRC in structural members under pure tensile loading is a function of the geometry of the element (length) and the apparent specific fracture energy decreases when the specimen's length increases.
- The introduction of a statistical scatter of the parameters of the tensile model of UHPFRC has a significant impact on the calculated mechanical response. The statistical variation of properties is an intrinsic feature of the materials and as such should be considered in the analysis of their mechanical response. Further research works are needed to study this topic and determine to which extend a statistical variation of the properties is a prerequisite to a sound modelling of the mechanical behaviour of UHPFRC.
- Significant eigenstresses are induced in UHPFRC layers applied on concrete substrates. Their intensity depends to a large extent on the degree of restraint (by the substrate and by reinforcement bars) of the overlay. For the investigated cases, with a moderate to high degree of restraint, the eigenstresses never reach the tensile strength of the UHPFRC. Further research is needed to investigate the case of structural elements with a very high degree of restraint.
- The eigenstresses can explain the apparent “weak” tensile response of UHPFRC obtained in recent research works, Habel (2004), through analytical inverse analysis of the fracture tests of composite structural members with UHPFRC.
- Sudden dimensional changes in the cross section of UHPFRC layers applied on concrete substrates induce significant stress concentrations.
- The models presented in this report can be combined to a later stage to study the interaction of eigenstresses and tensile fracture of UHPFRC in composite structural members at service state and ultimate limit state.

---

## 6. REFERENCES

Bazant Z. P., Oh B., (1983), Crack band theory for fracture of concrete, *Materials and Structures*, Vol. 16, No. 93, pp 155-177.

Bazant Z.P., Planas J., (1998) "Fracture and Size Effect in Concrete and Other Quasibrittle Materials", CRC Press LLC, pp. 220-227.

Bernard O., Comportement à long terme des éléments de structure formés de bétons d'âges différents, Doctoral Thesis, No. 2283, Swiss Federal Institute of Technology (EPFL), Lausanne, Switzerland, 2000, 190 p. (in French).

Bernard O., Brühwiler E., Influence of autogenous shrinkage on early age behaviour of structural elements consisting of concretes of different ages, *Materials and Structures*, Vol. 35, No. 235, November, 2002, pp 550-556.

Bernard O., Brühwiler E., The effect of reinforcement in the new layer on hygral cracking in hybrid structural elements, *Materials and Structures*, Vol. 36, No. 256, March, 2003, pp 118-126.

Bissonnette B., Pigeon M., Le comportement viscoélastique du béton en traction et la compatibilité déformationnelle des réparations, *Materials and Structures*, Vol. 33, No. 226, March, 2000, pp 108-118 (in French).

AFGC/SETRA (2002), « Bétons Fibrés à Ultra Hautes Performances », Recommandations provisoires, éditées par Association Française de Génie Civil et Service Technique des Routes et des Autoroutes, ref. SETRA: F0211.

Denarié E., (2005), "Structural rehabilitations with Ultra-High Performance Fibre Reinforced Concretes (UHPFRC)", ICCR 2005: International Conference on Concrete repair, rehabilitation and retrofitting, 21-23, November 2005, Cape Town, South Africa, 21-23 Novembre 2005 - Keynote Lecture. Eds.: M. Alexander, H.-D. Beushausen, F. Dehn, P. Moyo, Taylor & Francis, London (book with extended summaries and CD-ROM with full papers).

Dugat J., Roux N., Bernier G., (1996), Mechanical Properties of Reactive Powder Concretes, *Materials and Structures*, Vol. 29, No. 188, pp 233-240.

Habel K.: Structural behaviour of composite "UHPFRC-concrete" elements, Doctoral thesis, Swiss Federal Institute of Technology, Lausanne, Switzerland, 2004.

Habel K., Charron J.P., Denarié E., Brühwiler E., (2006a), Autogenous deformations and viscoelasticity of UHPFRC in structures – Part I: Experimental results, *Magazine of Concrete Research*, 58, No. 3, April 2006 pp.135–145.

---

Habel K., Charron J.P., Denarié E., Brühwiler E., (2006b), Autogenous deformations and viscoelasticity of UHPFRC in structures –Part II: Numerical Modelling, Magazine of Concrete Research, 58, No. 3, April 2006, pp.147-156.

Hillerborg A., (1983), Analysis of a single crack, Fracture mechanics of concrete, Ed. By F.H.Wittmann, Elsevier science Publishers B.V., Amsterdam, Netherlands, pp 223-249.

Kamen A., Denarié E., Brühwiler E., (2005), Mechanical Behaviour of Ultra High Performance Fiber Reinforced Concretes (UHPFRC) at early age, and under restraint, Proceedings CONCREEP 7, September 12-14, 2005 – Nantes, France, Eds. G. Pijaudier-Cabot, B. Gérard, P. Acker, Hermès Publishing, pp. 591-596.

Laurence O., (2001), La fissuration due au retrait restreint dans les réparations minces en béton: apports combinés de l'expérimentation et de la modélisation, thèse de doctorat de l'École Nationale des Ponts et Chaussées, Paris, France, Philosophiae Doctor (Ph.D.) de l'Université Laval, Quebec, Canada (in French).

Martinola G., (2000), Rissbildung und Ablösung zementgebundener Beschichtungen auf Beton. Diss. Technische Wissenschaften ETH Zürich, Nr. 13520, <http://e-collection.ethbib.ethz.ch/ecol-pool/diss/fulltext/eth13520.pdf>

Martinola G., Sadouki H., Wittmann F.H., (2001), Numerical model for minimizing the risk of damage in repair system, ASCE Journal of Materials in Civil Engineering, March/April 2001, pp. 121-129.

Rasmussen, R. O., B. F. McCullough, and J. Weissmann, (1995), Development of a Bonded Concrete Overlay Computer-Aided Design System, Research Report 2911-1, Center for Transportation Research, The University of Texas at Austin, January.

Roelfstra P. E., Salet A. M., Kuiks J. E. (1994) Defining and application of stress-analysis-based temperature difference limits to prevent early-age cracking in concrete structures. Proceedings n°25 of the International RILEM Symposium: Thermal cracking in concrete at early age, pp. 273-280. Munich.

Rossi, P. 2000. Ultra-High Performance Fibre Reinforced Concretes (UHPFRC): an overview. In P. Rossi and G. Chanvillard (eds) Proceedings of the Fifth International RILEM Symposium on Fibre-Reinforced Concretes, BEFIB'2000: 87-100, Lyon, France.

Rossi, P. 2002. Development of new cement composite material for construction. In K. Dhir, P. C.Hewlett, L. J. Csetenyi (eds) Proceedings of the International Conference on Innovations and Developments In Concrete Materials And Construction: 17-29, University of Dundee, Dundee, Scotland.

Rostasy F.S., Kraus M., Budelmann H., (2002), "Planungswerkzeug zur Kontrolle der frühen Rissbildung in massigen Betonbauteilen – Teil 5: Behinderung und Zwang", Bautechnik 79, Heft 11, pp. 778-789"

Naaman A., (2003), Strain hardening and deflection hardening fiber reinforced cement composites, in Proceedings HPFRCC4, Edited by A.E. Naaman and H.W. Reinhardt RILEM publications, Proceedings Pro 30, pp. 95-113.

Parant, E, (2003), Mécanismes d'endommagement et comportements mécaniques d'un composite cimentaire fibré multi-échelles sous sollicitations sévères: fatigue, choc, corrosion. Ph.D. thesis of Ecole nationale des Ponts et Chaussées, Paris (in French).

SAMARIS D13, (2004), Report on preliminary studies for the use of HPFRCC for the rehabilitation of road infrastructure components, European project 5th FWP / SAMARIS – Sustainable and Advanced MAterials for Road Infrastructures – WP 14: HPFRCC, <http://samaris.zag.si/>.

SAMARIS D18a, (2005), Report on laboratory testing of UHPFRC, part a, European project 5th FWP / SAMARIS – Sustainable and Advanced MAterials for Road Infrastructures – WP 14: HPFRCC, <http://samaris.zag.si/>.

SAMARIS D18b, (2006), Report on laboratory testing of UHPFRC, part b., European project 5th FWP / SAMARIS – Sustainable and Advanced MAterials for Road Infrastructures – WP 14: HPFRCC, <http://samaris.zag.si/>.

SAMARIS D22, (2005), Full scale application of UHPFRC for the rehabilitation of bridges – from the lab to the field, European project 5th FWP / SAMARIS – Sustainable and Advanced MAterials for Road Infrastructures – WP 14: HPFRCC, <http://samaris.zag.si/>.

SAMARIS D25b, (2006), Guidance for the use of UHPFRC for rehabilitation of concrete highway structures, European project 5th FWP / SAMARIS – Sustainable and Advanced MAterials for Road Infrastructures – WP 14: HPFRCC, <http://samaris.zag.si/>.

Wuest J. (2004a) Etude Exploratoire des Propriétés Mécaniques de Bétons de Fibres Ultra Performants de Structures, Diploma thesis, MCS, Swiss Federal Institute of Technology (EPFL), Lausanne, Switzerland, (in French).

Wuest J., (2004b), Flexural tests on UHPFRC plates, internal report, MCS, Lausanne.

---

## List of Figures

Figure 1: Concept of application of UHPFRC for the rehabilitation of reinforced concrete structures.....	11
Figure 2: : a)Tensile behaviour of two UHPFRC recipes, CEMTEC <sub>multiscale</sub> ®, b)comparison of tensile behaviour of UHPFRC CM23 with other materials.....	14
Figure 3: Tensile behaviour of HPFRCC-UHPFRC and comparison with FRC and concrete, after Naaman (2003).....	15
Figure 4: Crack band model of Bazant and Oh (1983), generalization to materials with significant bulk dissipation, Bazant and Planas (1998).....	17
Figure 5: Constitutive tensile law for a finite element of size $h_c$ , c) snapback effect of the scaling of the softening branch, due to oversized finite element.....	18
Figure 6: Schematic representation of the dogbone-shaped specimen, its subdivision in macro-elements, supports and loading point, as given by the graphical pre-processor of MLS.....	19
Figure 7: Stress-strain hardening-softening of the material as introduced and visualized in MLS-FE Code, the stresses are normalized to the tensile strength ( $\sigma_{cc}$ ) ( $L_{vol}$ : 430mm).....	20
Figure 8: FE-idealizations of the dogbone-shaped tensile test specimens with three different FE-sizes: a) 5, b) 10 and c) 20 mm.....	20
Figure 9: Evolution of damage distribution in the specimens at 4 increasing load-levels: a) 1.30, b) 1.40, c) 2.00 and d) 4.00 mm.....	21
Figure 10: Deformed shapes showing the widening of the microcracked band at an advanced load level (2 mm).....	22
Figure 11: Simulated stress-deformation responses for the model with three different mesh refinements.....	22
Figure 12: Example of statistical variation of the stress-strain hardening softening law, the solid diagram represents the mean curve( $\mu$ ) and dashed diagrams are curves with lowest value ( $\mu-\sigma$ ) and highest value ( $\mu+\sigma$ ), ( $\mu$ and $\sigma$ are the mean value of the tensile strength and the standard deviation).....	24
Figure 13: Comparison between simulated response of the dogbone-shaped test specimens with and without statistical distribution of the hardening and softening tensile strengths.....	25
Figure 14: Comparison of damage distribution and evolution during hardening phase for the case with constant material parameters (left, a and c) and for the case with statistically distributed tensile strengths (right, b and d) at two different load-levels: 1.3 mm (a and b) and 4 mm (c and d).....	26
Figure 15: Localisation of microcracked bands (real cracks, shown by arrows) in the specimens at an imposed displacement of 2mm, (a) homogeneous,	

---

(b) statistically distributed tensile strengths. ....	27
Figure 16: Comparison of the tensile behaviour by using different statistical distributions of the parameters of the stress-strain hardening-softening law (tensile strengths and characteristic hardening volume length (Lvol)). ....	28
Figure 17: Dogbone tensile test specimens with increasing lengths: 100, 300, 900, 1800 and 3600mm, from down to up, respectively. Thickness constant (100mm) .....	29
Figure 18: Evolution of damage induced during the hardening phase in the 5 dogbone-shaped tensile test specimens during the hardening phase at four displacement levels: (a) 0.6, (b) 2, (c) 4 and (d) 6mm. ....	30
Figure 19: Simulated stress-displacement curves for dogbone-shaped tensile specimens with different lengths (1): 100mm, (2): 300mm, (3): 900mm; (4): 1800mm and (5): 3600mm. ....	31
Figure 20: Stress Crack Opening Displacement (COD) as function of the specimen length deduced from the simulated stress-displacement curves shown in Figure 19. ....	31
Figure 21: Fracture energy ( $G_F$ ) and magnitude of hardening (MH) as function of the length of the specimen. ....	32
Figure 22: Comparison of the simulated stress-displacement curves between the case of a homogeneous material (black curves) and the case of statistically distributed tensile strengths (blue curves). ....	32
Figure 23: Magnitude of the hardening domain as function of the length of the specimen for a homogeneous material and for a material with statistically distributed tensile strengths. ....	33
Figure 24: Deduced stress-crack opening displacement (COD) diagrams, (softening regime).....	34
Figure 25: Comparison of the evolution of the fracture energy ( $G_F$ ) with the length of the specimen for both “homogeneous material model” and “statistically distributed tensile strengths model”. ....	34
Figure 26: Comparison between damage induced during the hardening phase at an imposed displacement of 4 mm: (a) constant material parameters, (b) statistically distributed tensile strengths. ....	35
Figure 27: Experimental set-up for 4-point bending tests on plates, Wuest (2004a).....	38
Figure 28: Geometrical and loading configuration of the UHPFRCC monolithic beams and its subdivision in macro-elements. ....	38
Figure 29: Comparison between the experimental (average curve) and fitted Force-deflection curves for the material CM23 cured at 20 <sup>0</sup> C at an age of 28 days, Wuest (2004b). ....	39
Figure 30: Resulting stress-displacement hardening-softening laws for material CM23 cured at 20 <sup>0</sup> C at an age of 28 days, deduced from back analyse (Figure 29) and experimental curves obtained from uniaxial	

---



tension specimen, SAMARIS D22 (2005).....	40
Figure 31: Schematic representation of the 3-point bending beams used to determine mechanical properties of DUCTAL® (A and C) .....	41
Figure 32: Distribution of damage in the material DUCTAL®-A at imposed displacement levels of: a) 0.2, b) 0.3mm and c) 0.6. ....	41
Figure 33: Comparison between experimental and numerical force-deflection curves of DUCTAL®-A bending beam and evolution of stresses at the bottom and in the centre of the specimen (Lvol: 200mm).....	42
Figure 34: Comparison between experimental and numerical force-deflection curves of DUCTAL®-C bending beam and evolution of stresses at the bottom and in the centre of the specimen; (Lvol: 200mm).....	43
Figure 35: Stress-strain hardening softening diagrams for two UHPFRC obtained from experimental curves by means of an inverse analysis. (volumetric characteristic length Lvol= 200 mm). ....	44
Figure 36: Actions, effects, and main parameters in a composite structural member with cementitious materials of different ages. ....	47
Figure 37: Schematic representation of the composite UHPFRC-concrete beams used in experimental investigations.....	48
Figure 38: Positions and dimensions of the steel reinforcement bars in a cross section (a) in the substrate, (b) in the composite beam, SMARIS D18b (2006).49	49
Figure 39: Measured heat of hydration under semi-adiabatic condition and comparison with Danish model obtained by means of numerical analysis, SAMARIS D22 (2005). ....	50
Figure 40: Measured free autogenous shrinkage for UHPFRCC CM22. Note: the setting delay of 30 hours for the start of the autogenous shrinkage has been considered but cannot be seen on the figure.....	51
Figure 41: Visualisation of the mesh of a part of the slender composite beam. It is composed on 2842 F.E. with different sizes (overlay in green, substrate in blue) and on 203 interfacial elements along the interface between the overlay and the substrate.....	52
Figure 42: Position of steel reinforcement bars (black in the substrate and red in the UHPFRCC-overlay).....	52
Figure 43: Partial view of the deformed shapes of the composite beam at 12, 28 and 72 hours after the casting operation. ....	53
Figure 44: Evolution at short term (3 days) of the mid and end-span deformations of the composite beam induced by thermal effects (liberation of heat of hydration in UHPFRCC and surrounding temperature) and self-desiccation of the overlay.....	54
Figure 45: Evolution at a middle term (6 months) of the mid and end-span deformations of the composite beam induced mostly by the autogenous shrinkage of the UHPFRCC.....	54

---

Figure 46:	Stress distribution in the left part of the slender composite beam at two ages (a) 30 d and (b) 180 d. UHPFRCC overlay with a thickness of 50mm and reinforced by steel bars. The lower face of the system is supported vertically by two point-supports only. ....	55
Figure 47:	Evolution of the highest autogenous shrinkage-induced eigenstress in the UHPFRCC-overlay and of the tensile strength ( $\sigma_{cc}$ ) of the material as function of age. The curve obtained by considering UHPFRCC as linear elastic material is also plotted in order to underline the beneficial effect of the viscoelastic character of UHPFRCC. ....	55
Figure 48:	Stress distribution in the left part of the composite beam at an age of 6 months. UHPFRCC overlay with a thickness of 50mm and reinforced by steel bars: (a) lower face of the system is simply supported vertically at two rolling pins, (b) lower face of the substrate totally restrained. ....	56
Figure 49:	Comparison of the evolution of the highest autogenous shrinkage-induced eigenstress in the UHPFRCC-overlay as function of age between two cases of restraint of the lower face of the substrate: totally restrained, restrained vertically at 2 points (by means of rolling pins). ....	56
Figure 50:	Stress distribution in the left part of the composite beam at an age of 6 months. UHPFRCC overlay with a thickness of 50mm (a) without steel bar reinforcement, (b) with steel bar reinforcement. ....	57
Figure 51:	Comparison of the evolution of the highest autogenous shrinkage-induced eigenstress in the UHPFRCC-overlay (thickness 50mm) as function of age between two cases: with and without steel bars reinforcement of the overlay. ....	57
Figure 52:	Evolution at a middle term (6 months) of the mid and end-span deformations of the composite beam induced by the autogenous shrinkage of the UHPFRCC-overlay with a thickness of 50mm, with and without steel bars reinforcement. ....	58
Figure 53:	Evolution at a middle term (6 months) of the mid and end-span deformations of the composite beam induced by the autogenous shrinkage of the UHPFRCC-overlay with two different thicknesses: 20 and 50mm. ....	59
Figure 54:	Comparison of the evolution of the highest tensile stress in the UHPFRCC with two different thicknesses (30 and 50mm) for two degrees of restraint. ....	59
Figure 55:	Schematic representation of a composite UHPFRCC-concrete beam with an over-depth. ....	60
Figure 56:	Autogenous shrinkage-induced stress distribution in a composite UHPFRCC-concrete beam presenting an over-depth, at three different ages (3, 30 and 100days). ....	61
Figure 57:	Stress evolution in the composite UHPFRCC-concrete beam with an over-depth at different points. ....	61